

## A DYNAMICAL STUDY OF EXTRAPLANAR DIFFUSE IONIZED GAS IN NGC 5775\*

ERIN BOETTCHER<sup>1,2</sup>, J. S. GALLAGHER III<sup>1</sup>, ELLEN G. ZWEIBEL<sup>1,3</sup>

<sup>1</sup>Department of Astronomy, University of Wisconsin - Madison, 475 North Charter Street, Madison, WI 53706, USA

<sup>2</sup>Department of Astronomy & Astrophysics, University of Chicago, 5640 S. Ellis Avenue, Chicago, IL 60637, USA;  
eboettcher@astro.uchicago.edu and

<sup>3</sup>Department of Physics, University of Wisconsin - Madison, 1150 University Avenue, Madison, WI 53706, USA

*Draft Version September 27, 2019*

### ABSTRACT

The structure and kinematics of gaseous, disk-halo interfaces are imprinted with the processes that transfer mass, metals, and energy between galactic disks and their environments. We study the extraplanar diffuse ionized gas (eDIG) layer in the interacting, star-forming galaxy NGC 5775 to better understand the consequences of star-formation feedback on the dynamical state of the thick-disk interstellar medium (ISM). Combining emission-line spectroscopy from the Robert Stobie Spectrograph on the Southern African Large Telescope with radio continuum observations from Continuum Halos in Nearby Galaxies - an EVLA Survey, we ask whether thermal, turbulent, magnetic field, and cosmic-ray pressure gradients can stably support the eDIG layer in dynamical equilibrium. This model fails to reproduce the observed exponential electron scale heights of the eDIG thick disk and halo on the northeast ( $h_{z,e} = 0.6, 7.5$  kpc) and southwest ( $h_{z,e} = 0.8, 3.6$  kpc) sides of the galaxy at  $R < 11$  kpc. We report the first definitive detection of an increasing eDIG velocity dispersion as a function of height above the disk. Blueshifted gas along the minor axis at large distances from the midplane hints at a disk-halo circulation and/or ram pressure effects caused by the ongoing interaction with NGC 5774. This work motivates further integral field unit and/or Fabry-Perot spectroscopy of galaxies with a range of star-formation rates to develop a spatially-resolved understanding of the role of star-formation feedback in shaping the kinematics of the disk-halo interface.

*Subject headings:* galaxies: individual(NGC 5775) — galaxies: ISM — ISM: kinematics and dynamics

### 1. INTRODUCTION

In Milky Way-type galaxies, the gaseous, disk-halo interface is shaped by processes that regulate the growth of galaxies at low redshift. These processes include star-formation feedback, which drives galactic fountains (Shapiro & Field 1976; Bregman 1980) and galactic winds (e.g., Veilleux et al. 2005), as well as cold gas accretion necessary to sustain star formation over cosmic lifetimes (e.g., Larson et al. 1980). Well known galaxy scaling relationships, including the stellar-mass - halo-mass and mass-metallicity relations (e.g., Silk 2003; Tremonti et al. 2004), suggest that mass, metals, and energy cycle through the disk-halo interface in ways that have important implications for galaxy evolution.

These observations motivate a careful study of the vertical structure, support, and kinematics of the gaseous, disk-halo interfaces of nearby galaxies. A long-standing challenge to our understanding of the dynamical state of the thick-disk interstellar medium (ISM) is the presence of extraplanar diffuse ionized gas (eDIG) layers in the Milky Way and other star-forming galaxies. Vertically-extended, photoionized, diffuse ( $T \sim 10^4$  K,  $\langle n_{e,0} \rangle \sim 0.1$  cm<sup>-3</sup>) gas is observed in galaxies with star-formation rates comparable to or exceeding that of the Galaxy (Lehnert & Heckman 1995; Rossa & Dettmar 2003). A particularly puzzling feature of eDIG layers is that their observed exponential electron scale heights ( $h_{z,e} \sim 1$  kpc) exceed their thermal scale heights ( $h_{z,e,th} \sim 0.2$

kpc) by factors of a few in the Milky Way (Haffner et al. 1999) and nearby, edge-on disk galaxies (e.g., Rand 1997; Collins & Rand 2001). As yet, the large scale heights of eDIG layers have defied full explanation with ballistic (e.g., Collins et al. 2002) and (magneto)hydrodynamic models (e.g., Hill et al. 2012).

A simple question that can be asked is whether there is sufficient vertical pressure to stably support eDIG layers in dynamical equilibrium if turbulent, magnetic field, and cosmic-ray pressure gradients are invoked in addition to the thermal pressure gradient. While dynamical equilibrium has been considered as a viable model for the vertically-extended ISM in the Milky Way (Boulares & Cox 1990; Fletcher & Shukurov 2001), this question has only recently been considered in detail for eDIG layers in external galaxies. Boettcher et al. (2016) demonstrated that thermal and nonthermal pressure gradients are only capable of stably supporting the eDIG layer in NGC 891 at large galactocentric radii ( $R \geq 8$  kpc). However, application of such analysis to other galaxies is desired, including those with differing star-formation rates and interaction histories. In the absence of dynamical equilibrium, it is then apt to ask whether there is kinematic evidence for a nonequilibrium process such as a galactic fountain, wind, or accretion flow.

Here, we perform a dynamical study of the eDIG layer in the nearby, edge-on disk galaxy NGC 5775 (SBc? sp; de Vaucouleurs et al. 1991). This well-studied, star-forming galaxy is viewed at an inclination angle of  $i = 86^\circ$  (Irwin 1994), and we adopt a distance of  $D = 28.9$  Mpc ( $1'' = 0.14$  kpc; Irwin et al. 2012). NGC 5775 has an *IRAS* far-infrared surface brightness of  $L_{FIR}/D_{25}^2 =$

\*Based on observations made with the Southern African Large Telescope (SALT) under programs 2015-1-SCI-023 and 2016-2-SCI-029 (PI: E. Boettcher).

$8.4 \times 10^{40}$  erg  $s^{-1}$   $kpc^{-2}$  that is consistent with the more quiescent of starburst systems (Collins et al. 2000; Rossa & Dettmar 2003). One of its most notable features is its interaction with companion galaxy NGC 5774; there is evidence that this barred spiral galaxy is donating neutral hydrogen gas to NGC 5775 via an HI bridge characterized by Irwin (1994), enhancing the star-formation rate of the latter galaxy. NGC 5775 has a spatially-extended, multiphase gaseous halo whose structure and kinematics shed light on the disk-halo connection in star-forming systems (e.g., Irwin 1994; Rand 2000; Tüllmann et al. 2006; Li et al. 2008).

The structure, ionization, and kinematics of the eDIG layer in NGC 5775 have been the subject of extensive study. Narrow-band imaging reveals a highly filamentary eDIG layer superimposed on a diffuse background (Collins et al. 2000). This galaxy has one of the most vertically-extended emission-line halos known; Rand (2000) detected emission to  $z = 15$  kpc, corrected for our choice of  $D$ . The evolution of the emission-line ratios with height above the disk suggests the presence of a supplementary source of heating and/or ionization in addition to photoionization, such as shocks or turbulent mixing layers (e.g., Tüllmann et al. 2000; Collins & Rand 2001; Otte et al. 2002). The interplay, if any, between dynamical processes in the eDIG and supplementary sources of heating and ionization remains an open question. Heald et al. (2006) probe the kinematics of the eDIG layer using Fabry-Perot spectroscopy, revealing a rotational velocity lag in the extraplanar gas within a few kiloparsecs of the disk.

Consideration of the role of extraplanar magnetic fields and cosmic rays in the dynamics, heating, and/or ionization of the eDIG in NGC 5775 is motivated by the detection of an extensive ( $z \sim 12 - 17$  kpc, corrected for  $D$ ) radio continuum halo (Duric et al. 1998). More recently, the synchrotron halo of NGC 5775 has been studied by Continuum Halos in Nearby Galaxies - an EVLA Survey (CHANG-ES). A goal of this program is to characterize the nonthermal halos of 35 nearby, edge-on disk galaxies at 1.5 and 6 GHz with the Karl G. Jansky Very Large Array (Irwin et al. 2012; Wiegert et al. 2015). A Faraday rotation study by Soida et al. (2011) examined the large-scale structure of the magnetic field in NGC 5775, revealing a plane-parallel field close to the disk and an increasingly X-shaped field in the halo. Collins et al. (2000) present evidence for a spatial correlation between H $\alpha$  filaments, HI shells, and radio continuum “spurs” suggestive of a galactic chimney model. These correlations motivate a better understanding of how gas, magnetic fields, and cosmic rays are transported by disk-halo flows and whether or not they are able to achieve a mutual equilibrium state.

This paper is presented as follows. In §2, we describe the collection, reduction, and analysis of optical and near-ultraviolet (NUV) longslit spectroscopy obtained with the Robert Stobie Spectrograph (RSS) on the Southern African Large Telescope (SALT). In §3.1, we characterize the eDIG density distribution, and we discuss the emission-line ratios and their implications for the physical conditions in the eDIG layer in §3.2. We describe the radial velocities and velocity dispersions in §3.3. In §4, we develop and test a dynamical equilibrium model of the eDIG layer and consider whether it

TABLE 1  
NGC 5775 OBSERVING SUMMARY

Slit Label	R.A. <sup>a</sup> (J2000)	Decl. <sup>a</sup> (J2000)	P.A. <sup>b</sup> (deg)	$t_{exp}$ (s)
s1	14 53 57.6	+03 32 40	55.7	$5 \times 1600$
s2	14 53 56.2	+03 32 26	145.7	$4 \times 1615$
s3uv	14 53 56.0	+03 33 20	55.7	$3 \times 1670$
s3o	14 53 56.0	+03 33 20	55.7	$2 \times 1660$

<sup>a</sup> The R.A. and decl. at the center of the slit. R.A. is measured in hours, minutes, and seconds; decl. is measured in degrees, arcminutes, and arcseconds.

<sup>b</sup> The position angle measured from north to east.

is robust against the Parker instability. We discuss our results in the context of the literature in §5 and conclude with motivation for future observations in §6.

## 2. OBSERVATIONS

### 2.1. Data Collection

We used the optical and NUV capabilities of RSS (Burgh et al. 2003; Kobulnicky et al. 2003) in longslit mode on SALT (Buckley et al. 2006). We placed one slit on the minor axis (PA = 55.7°, s1) and a second slit parallel to the major axis and offset by  $\Delta z = 3.5$  kpc on the southern side of the galaxy (PA = 145.7°, s2; see Fig. 1). We used a 1.25" width for the 8' longslits and the pg2300 grating at an angle of 48.875°. This produced a dispersion of 0.26 Å pixel<sup>-1</sup>, a spectral resolution of  $R = 4830$  ( $\sigma = 26$  km s<sup>-1</sup>) at H $\alpha$ , and wavelength coverage from 6100 Å to 6900 Å, including the [NII] $\lambda\lambda 6548, 6583$ , H $\alpha$ , and [SII] $\lambda\lambda 6717, 6731$  emission lines. We obtained these data between 2017 February 23 and 2017 March 04.

We also placed a slit perpendicular to the disk at  $R = 6.5$  kpc on the northwest side of the galaxy (PA = 55.7°, s3; see Fig. 1). This slit falls along a bright filament detected in H $\alpha$  imaging by Collins et al. (2000). We obtained two sets of observations at this location: moderate spectral resolution observations of the [OII] $\lambda\lambda 3726, 3729$  emission-line doublet (s3uv), and low spectral resolution observations with wavelength coverage from [OII] $\lambda\lambda 3726, 3729$  to [NII] $\lambda\lambda 6548, 6583$  (s3o). The [OII] doublet is a powerful eDIG tracer because it is comparably bright to H $\alpha$  (e.g., Otte et al. 2002) and is found in the NUV regime where the terrestrial sky foreground is minimal compared to the optical.

For the s3uv observations, a 1.5" slit width and the pg3000 grating at an angle of 34.25° yielded a dispersion of 0.24 Å pixel<sup>-1</sup> and a spectral resolution of  $R = 2400$  ( $\sigma = 53$  km s<sup>-1</sup>) at [OII]. For s3o, the pg0900 grating at an angle of 13.625° produced a dispersion of 0.97 Å pixel<sup>-1</sup> and a spectral resolution of  $R = 620$  ( $\sigma = 205$  km s<sup>-1</sup>) at [OII] and  $R = 1140$  ( $\sigma = 112$  km s<sup>-1</sup>) at H $\alpha$ . We obtained these observations between 2015 June 17 and 2015 August 06. For all data, we used  $2 \times 2$  on-chip binning to yield a plate scale of 0.25" pixel<sup>-1</sup>. We note the coordinates, position angles, and exposure times in Tab. 1.

### 2.2. Data Reduction

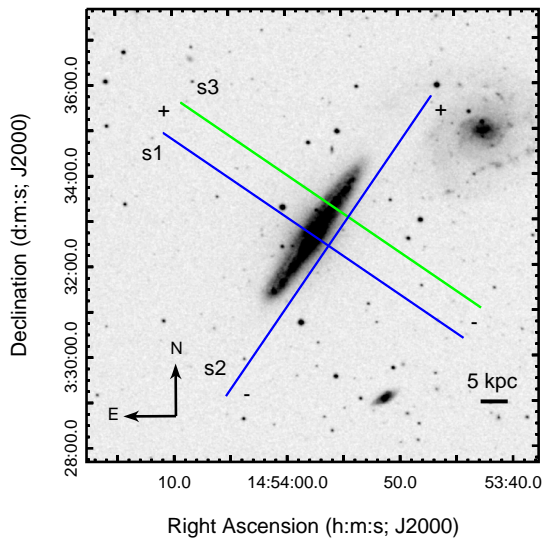


FIG. 1.— SALT-RSS longslits overlaid on a POSS2/UKSTU Red image of NGC 5775 from the Digitized Sky Survey (Second Generation; [http://stdu.stsci.edu/cgi-bin/dss\\_form](http://stdu.stsci.edu/cgi-bin/dss_form)). We obtained optical observations with moderate spectral resolution at the locations of the blue slits and NUV ( $[\text{OII}]\lambda\lambda 3726, 3729$ ; moderate resolution) and optical (low resolution) observations at the location of the green slit. The plus and minus signs indicate the sign conventions applied to the vertical ( $z$ ) and radial ( $R$ ) coordinates.

We performed the data reduction using a combination of the PySALT science pipeline<sup>1</sup> and IRAF software<sup>2</sup>. We utilized PySALT (Crawford et al. 2010) to apply the bias, gain, and cross-talk corrections as well as for the image preparation and mosaicking. Using the IRAF L.A. Cosmic package (van Dokkum 2001), we removed cosmic rays from the images. With the IRAF tasks `noao.twodspec.longslit.identify`, `reidentify`, `fitcoords`, and `transform`, we determined the dispersion solution using Ar comparison lamp spectra for s1 and s2. ThAr and Ar comparison lamp spectra were used for the low and moderate spectral resolution observations of s3.

In s1 and s2, there is a count background of currently unknown origin that varies along both the spatial and spectral axes. The presence of this background - identified as elevated counts above the bias - on both the illuminated and non-illuminated portions of the CCD chip confirm its origin as separate from the sky continuum. It contributes as much as 85% of the sky continuum at the blue end of the spectral range, but less than 20% of the sky continuum near the emission lines of interest. Due to the difficulty in separating the contributions from this background, the sky, and the galaxy, we fit and remove all three contributions to the continuum simultaneously. This is done by modeling the continuum pixel row by row in the spectral direction in the two-dimensional spectrum using a fifth-order Chebyshev function in the IRAF task `noao.twodspec.longslit.background`. We assume that the unidentified background, sky, and galaxy

continuum all contribute Poisson noise in the error estimation.

Our approach to sky-line subtraction differed depending on the slit position. For s1 and s3, we created median sky spectra from the ends of the slits that were free from galaxy emission. Before performing the sky subtraction, we scaled the sky spectrum by a multiplicative factor that we allowed to vary in the spatial dimension based on the relative strength of the sky lines across the slit. For s2, we did not know beforehand what fraction of the slit would be filled with galaxy emission. We thus obtained a single separate sky observation immediately following the first object observation along a telescope track that replicated the object track, exposure time, and instrument setup. Based on the relative intensities of the sky lines in the object and sky frames, we scaled the sky observation by a multiplicative factor before subtracting it from the object observations. Due to the count background mentioned previously, we fit and removed the continuum from both the sky and object frames before performing the sky-line subtraction.

We stacked the sky-subtracted science frames by aligning them in the spatial dimension based on the location of the peak  $\text{H}\alpha$  or  $[\text{OII}]$  emission. We then used the IRAF task `images.immatch.imcombine` to perform a median combine of the images with median scaling and weighting. To extract individual spectra, we performed a median combine over an aperture of 11 pixels; this is a compromise between optimizing the spatial resolution ( $\sim 385$  pc aperture<sup>-1</sup>) and the signal-to-noise ratio (S/N), while also mitigating the effects of the curvature of the spectral axis with respect to the CCD chip. We calculated the Poisson error on the raw data frames and propagated the uncertainty through the reduction and analysis.

### 2.3. Flux Calibration

Using observations obtained on 29 March 2016 and 25 February 2017, we performed the relative flux calibration for s3o and s1/s2 using the spectrophotometric standard stars Hiltner 600 and HR5501, respectively. No relative flux calibration was performed for s3uv due to the small wavelength range of interest around the  $[\text{OII}]$  doublet.

Absolute flux calibration cannot be performed with SALT alone due to the time-varying collecting area. We calibrated the  $\text{H}\alpha$  intensities along the minor axis using calibrated  $\text{H}\alpha$  narrow-band imaging obtained from the Hubble Legacy Archive<sup>3</sup> (PI: Rossa; Proposal ID: 10416). The observations were taken using ACS/WFC on the *Hubble Space Telescope* (*HST*) with the f658n filter. We convolved the image with a two-dimensional Gaussian with full width at half maximum (FWHM) equal to the average seeing at the SALT site (FWHM = 1.5'') using the IDL function `gauss_smooth`.

To determine the  $\text{H}\alpha$  calibration factor, we computed the mean flux over the bandpass for each extracted spectral aperture in the *HST* data using the PHOTFLAM keyword. We then compared this to the mean flux in the sky-subtracted SALT spectra convolved with the *HST* bandpass. We performed the analysis within  $|z| \leq 5$  kpc, but we restricted our determination of a median calibration factor to within  $|z| \leq 2$  kpc due to declining S/N at large  $z$ . The SALT-RSS slit width is sampled by 25 *HST*

<sup>1</sup> <http://pysalt.salt.ac.za/>

<sup>2</sup> IRAF is distributed by the National Optical Astronomy Observatories, which are operated by the Association of Universities for Research in Astronomy, Inc., under cooperative agreement with the National Science Foundation.

<sup>3</sup> <https://hla.stsci.edu/>

pixels, a sufficient number to avoid an infinite aperture correction. We do not account for uncertainty in the flux calibration in the error budget.

#### 2.4. Emission-line Detection and Fitting

We determined the detection limits for emission lines as follows. We identified statistically significant fluctuations in the spectra by first fitting and removing any remaining continuum; the fit was performed by masking emission lines and smoothing the spectrum with a broad Gaussian kernel ( $\sigma \gtrsim 15 \text{ \AA}$ ). We then divided the spectrum into intervals equal to the expected FWHM of the emission lines (FWHM = 2.5 - 6  $\text{\AA}$ ). Within each interval, we summed the counts per  $\text{\AA}$ ; we then fit the resulting distribution of integrated intensities with a Gaussian function and determined its standard deviation. We defined detections to be intervals whose integrated intensities were statistically significant at the  $5\sigma$  level.

We characterized the intensities, velocities, and velocity dispersions of detected emission lines by fitting them with single Gaussians using the IDL function `gaussfit`. The S/N does not permit reliable identification of multiple Gaussian components. The least-squares fitting routine also returns uncertainties on the best-fit parameters. In the Appendix, we show example spectra from s1, as well as the model fits and their residuals. We also include measured intensities, velocities, velocity dispersions, and emission-line ratios in online-only tables.

Due to partial blending of the [OII] doublet in the s3uv observations, we fit the doublet with a sum of two Gaussians by minimizing the  $\chi^2$  statistic over a parameter grid ( $\chi^2 = \sum \frac{(I_{\lambda,obs} - I_{\lambda,mod})^2}{\sigma_{obs}^2}$ , where  $I_{\lambda,obs}$  and  $I_{\lambda,mod}$  are the observed and modeled specific intensities and  $\sigma_{obs}$  is the uncertainty on the observed quantity). We judge by eye that the blended Gaussian fits are only reliable at detection levels of at least  $7\sigma$ , and thus we only report the results of these fits. The  $1\sigma$  error bars on the best-fit parameters were determined from the models within  $\chi^2 \leq \chi_{min}^2 + \Delta\chi^2$ , where  $\Delta\chi^2 = 3.53$  for three free parameters ( $\frac{I_{\lambda 3726}}{I_{\lambda 3726, 3729}}$ ,  $v_{[OII]}$ , and  $\sigma_{[OII]}$ ).

All emission-line widths reported in this paper are the standard deviations of the Gaussian fits and are corrected for the instrumental resolution determined from the comparison lamp spectra. The radial velocities are presented as heliocentric velocities calculated using the IRAF task `astutil.rvcorrect`. Line ratios are corrected for Galactic extinction using the reddening law of Cardelli et al. (1989) assuming  $R_V = 3.1$  and  $A(V) = 0.115$  (Schlafly & Finkbeiner 2011). We do not correct for internal extinction or for the underlying stellar absorption spectrum.

### 3. RESULTS

We detect one or more emission lines to spatial extents of  $-7.3 \text{ kpc} \leq z \leq 8.0 \text{ kpc}$  in s1, to  $-8.5 \text{ kpc} \leq z \leq 10 \text{ kpc}$  in s3o, and to  $-11.6 \text{ kpc} \leq R \leq 13.5 \text{ kpc}$  in s2. In s3uv, we detect [OII] emission to  $-8.5 \text{ kpc} \leq z \leq 7.3 \text{ kpc}$ ; detections at the  $7\sigma$  level or higher required for a reliable fit are restricted to  $|z| \leq 5.8 \text{ kpc}$  (see §2.4). Here,  $z$  is the vertical coordinate, where positive  $z$  is on the northeast side of the disk and negative  $z$  is on the southwest side. We choose  $z = 0$  to correspond to the main dust lane

in the disk, and we do not correct for inclination angle.  $R$ , the radial coordinate, is defined to be positive and negative west and east of the minor axis, respectively (see labels in Fig. 1).

#### 3.1. H $\alpha$ Intensity Profile

We fit the H $\alpha$  intensity,  $I_{H\alpha}$ , as a function of height,  $z$ , along the minor axis. The goal of the fitting is to determine the eDIG electron density,  $n_e(z)$ , and the exponential electron scale height,  $h_{z,e}$ . Since our observations are integrated in galactocentric radius and  $n_e(z)$  and  $h_{z,e}$  may depend on  $R$ , we take the best-fit values of these parameters as representative of their characteristic values. We perform the fit along the minor axis because H $\alpha$  imaging indicates a lack of filamentary structure at this location (Collins et al. 2000), giving us the best sense of the vertical structure of the diffuse layer.

We exclude observations within  $|z| \leq 1 \text{ kpc}$  to avoid contamination by HII regions, dust extinction, and underlying stellar absorption in the disk. There is evidence for extraplanar dust in NGC 5775, including PAH and H $_2$  emission with scale heights of  $\sim 0.7 - 1.1 \text{ kpc}$  (Rand et al. 2011). Molecular gas and dust are also detected to  $|z| \leq 5 \text{ kpc}$  in discrete locations that appear to coincide with HI supershells (Lee et al. 2002; Brar et al. 2003); however, no such features are seen along the minor axis at the location of s1. Thus, we assume that the impact of dust extinction on the measured eDIG scale height and density distribution above  $|z| \sim 1 \text{ kpc}$  is minor.

We perform the fitting using the IDL function `mpfitfun`. This routine performs a Levenberg-Marquardt least-squares fit of a user-supplied function to a data set. We fit a single exponential function of the form:

$$I_{H\alpha}(z) = I_{H\alpha}(0)e^{-|z|/h_z}, \quad (1)$$

as well as a double exponential function given by:

$$I_{H\alpha}(z) = I_{H\alpha,1}(0)e^{-|z|/h_{z,1}} + I_{H\alpha,2}(0)e^{-|z|/h_{z,2}}. \quad (2)$$

Here,  $I_{H\alpha}(0)$  is the intensity of the eDIG layer at  $z = 0 \text{ kpc}$  and  $h_z$  is the emission scale height. We associate components 1 and 2 with the thick disk and the halo, respectively. As shown in Fig. 2, the double exponential provides a much better fit to the intensity profile than the single exponential at large  $z$ .

From the  $I_{H\alpha}(z)$  profile, we can estimate  $n_e(z)$  as follows.  $I_{H\alpha}(z)$  depends on  $n_e(z)$ , the electron temperature,  $T_4$ , and the volume filling factor,  $\phi$ , according to:

$$I_{H\alpha}(z) = \frac{\int \phi n_e(z)^2 dl}{2.75T_4^{0.9}}. \quad (3)$$

Using standard units for the emission measure,  $I_{H\alpha}(z)$  is measured in Rayleighs,  $\phi n_e^2$  is given in  $\text{cm}^{-6}$ ,  $T_4$  has units of  $10^4 \text{ K}$ , and the integral is performed over the line of sight ( $\int dl = L$  for  $L$  in parsecs) (e.g., Haffner et al. 1998).

If  $\phi$  and  $n_e$  are assumed to be constant along a given line of sight, then we can express the observable quantity  $\phi n_e(z)^2$  as:

$$\phi n_e(z)^2 = \frac{I_{H\alpha}(z)(2.75T_4^{0.9})}{L}. \quad (4)$$

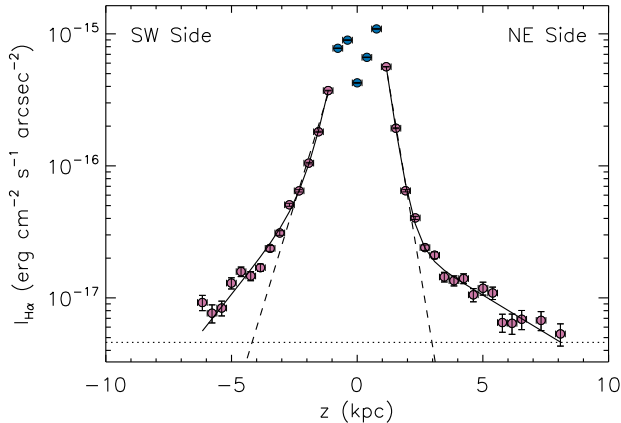


FIG. 2.— Best-fit, one-component (dashed lines) and two-component (solid lines) models of  $I_{H\alpha}$  as a function of  $z$  along the minor axis (s1). Best-fit parameters are given in Tab. 2. Pink points ( $|z| > 1$  kpc) are included in the fit. The dotted line indicates the detection threshold. The slight inclination of the galaxy from edge-on may contribute to the asymmetry in the  $I_{H\alpha}$  profile between the northeast and southwest sides of the disk.

We take the radial extent of the eDIG layer determined by Collins et al. (2000),  $R = 14$  kpc, to estimate  $L = 2R = 28$  kpc (note that  $R$  has been adjusted for  $D$ ).

We do not include any radial dependence, such as a radial scale length of the form  $n_e(R) \propto e^{-R/h_R}$ , for the derived densities. Evidence for such a dependence is not clear from existing imaging and spectroscopy. The  $H\alpha$  imaging of Collins et al. (2000) indicates that the eDIG morphology is largely filamentary, with local density enhancements dominating over large-scale trends. The radial density profile derived from Fabry-Perot spectroscopy by Heald et al. (2006) also suggests a clumpy rather than smooth structure. In light of this, we neglect a formal radial density dependence in our analysis and instead briefly consider the impact of including an eDIG radial scale length,  $h_R$ , on the success of the dynamical equilibrium model in §4.5.

The best-fit values of  $\phi n_e(0)^2$  and  $h_{z,e}$  for the single, thick disk, and halo components are given in Tab. 2. Note that due to the  $n_e^2$  dependence of  $I_{H\alpha}$ , the exponential electron scale height is twice the emission scale height, or  $2h_z = h_{z,e}$ . We quantify the uncertainties on the best-fit values of  $\phi n_e(0)^2$  and  $h_{z,e}$  by perturbing the values of  $I_{H\alpha}$  by increments randomly drawn from Gaussian distributions with standard deviations equal to their  $1\sigma$  error bars. We then refit the perturbed intensity profile and calculate the difference between the original and perturbed best-fit values. We repeat this process until the median differences converge ( $10^3$  iterations); these median values are the uncertainties reported in Tab. 2. Note that this approach does not account for systematic effects such as the deviation of the inclination angle from  $90^\circ$  and uncertainty in the flux calibration.

We also compare our best-fit parameters to past measurements of  $h_{z,e}$  and  $\phi n_e(0)^2$  in Tab. 3. Our scale heights are broadly consistent with the results of these single-component fits, although it is clear that variation exists as a function of  $R$ . Our minimum thick-disk scale height ( $h_{z,e} = 0.6$  kpc) and our maximum halo scale height ( $h_{z,e} = 7.5$  kpc) bracket existing measurements of

the scale height at various  $R$ . Thus, by testing a dynamical equilibrium model of each of our thick-disk and halo components both separately and together, we will assess the success of this model over a representative range of choices for  $h_{z,e}$ .

We estimate the total mass in the eDIG layer from the observed density distribution and an assumed volume filling factor. For  $\phi = 1$  ( $\phi = 0.1$ ), we find  $M_{eDIG} = 1.1 \times 10^{10} M_\odot$  ( $M_{eDIG} = 3.5 \times 10^9 M_\odot$ ) on the northeast side of the disk and  $M_{eDIG} = 8.4 \times 10^9 M_\odot$  ( $M_{eDIG} = 2.6 \times 10^9 M_\odot$ ) on the southwest side. 65% (54%) of the mass is found in the thick disk on the northeast (southwest) side. These exceed previous estimates of the masses of eDIG layers in other galaxies by more than an order of magnitude (e.g., Dettmar 1990; Boettcher et al. 2017). They are also comparable to the total HI mass ( $M_{HI} = 9.1 \pm 0.6 \times 10^9 M_\odot$ ; Irwin 1994) and more than the total hot halo mass ( $M_{hot} = 5.3 \times 10^8 M_\odot$ ; Li et al. 2008).

This suggests that we have overestimated the eDIG mass, implying the need for a very small volume filling factor. Assuming pressure equilibrium between the warm and hot phases does indeed imply an eDIG filling factor of  $\phi \sim 0.1$  (Li et al. 2008). Additionally, if the eDIG density decreases exponentially as a function of  $R$ , then a reasonable choice of radial scale length ( $h_R \sim 3 - 5$  kpc) decreases the total mass estimate by  $\sim 50\%$ .

### 3.2. eDIG Properties

We use the emission-line ratios to gain a qualitative sense of the physical conditions in the eDIG layer. The emission-line properties have been previously studied in detail by Tillmann et al. (2000), Collins & Rand (2001), Otte et al. (2002), and others; we confirm their findings at the location of s3, and expand on their results at the locations of s1 and s2. Note that internal extinction and underlying stellar absorption may affect observed line ratios at small  $z$ ; however, we emphasize interpretation of the line ratios at  $|z| \geq 1$  kpc, where we assume these effects are minimal.

The  $[OII]\lambda 3727/H\alpha$ ,  $[NII]\lambda 6583/H\alpha$ , and  $[SII]\lambda 6717/H\alpha$  line ratios depend on temperature, ionization fraction, and elemental abundance as follows (Haffner et al. 1999; Osterbrock & Ferland 2006):

$$\frac{I([OII]\lambda 3727)}{I(H\alpha)} = (4.31 \times 10^5) T_4^{0.4} e^{-3.87/T_4} \left(\frac{O^+}{O}\right) \left(\frac{O}{H}\right) \left(\frac{H^+}{H}\right)^{-1}, \quad (5)$$

$$\frac{I([NII]\lambda 6583)}{I(H\alpha)} = (1.62 \times 10^5) T_4^{0.4} e^{-2.18/T_4} \left(\frac{N^+}{N}\right) \left(\frac{N}{H}\right) \left(\frac{H^+}{H}\right)^{-1}, \quad (6)$$

and

$$\frac{I([SII]\lambda 6717)}{I(H\alpha)} = (7.67 \times 10^5) T_4^{0.307} e^{-2.14/T_4} \left(\frac{S^+}{S}\right) \left(\frac{S}{H}\right) \left(\frac{H^+}{H}\right)^{-1}. \quad (7)$$

We assume  $H^+/H \sim 1$  and  $N^+/N \sim 0.8$  under typical DIG conditions (Reynolds et al. 1998; Sembach et al. 2000). We also assume  $O^+/O = N^+/N$  given their similar first ionization potentials. Though the relatively high second ionization potentials of  $N$  and  $O$  (29.6 and 35.1 eV, respectively) suggest that  $N^{++}/N$  and  $O^{++}/O$  are low in the DIG, the lower second ionization poten-

TABLE 2  
 H $\alpha$  INTENSITY PROFILE

Model	$h_{z,e,1}$ (kpc)	$\phi n_{e,1}(0)^2$ ( $\text{cm}^{-6}$ )	$h_{z,e,2}$ (kpc)	$\phi n_{e,2}(0)^2$ ( $\text{cm}^{-6}$ )
Thick disk (SW)	$1.4 \pm 0.009$	$0.029 \pm 0.0004$	—	—
Thick disk (NE)	$0.8 \pm 0.04$	$0.184 \pm 0.003$	—	—
Thick disk + halo (SW)	$0.8 \pm 0.04$	$0.069 \pm 0.004$	$3.6 \pm 0.2$	$0.003 \pm 0.0004$
Thick disk + halo (NE)	$0.6 \pm 0.04$	$0.302 \pm 0.007$	$7.5 \pm 0.4$	$0.0006 \pm 0.00004$

 TABLE 3  
 PAST MEASUREMENTS OF ELECTRON SCALE HEIGHT AND DENSITY

$h_{z,e}$ (kpc)	$\phi n_e(0)^2$ ( $\text{cm}^{-6}$ )	Location	Reference <sup>a</sup>
1.6 - 1.8	0.0065 - 0.01	$R = 0 - 2$ kpc ( $-z$ )	[1]
1.8	0.0055	$R = -(8 - 10)$ kpc	[1]
6.0	—	H $\alpha$ filament (NE side)	[1]
5.0	—	H $\alpha$ filaments (SE, SW sides)	[1]
4.6	—	$R = 4.5$ kpc ( $+z$ )	[2]
4.6	—	$R = 4.5$ kpc ( $-z$ )	[2]
5.0	—	$R = -2.8$ kpc ( $+z$ )	[2]
3.6	—	$R = -2.8$ kpc ( $-z$ )	[2]
1.6	—	SW side	[3]
1.2	—	NE side	[3]

<sup>a</sup> References: [1] - Collins et al. 2000; [2] - Collins & Rand 2001; [3] - Heald et al. 2006

tial of  $S$  (23.3 eV) means that  $S^{++}/S$  may be considerable. Thus, we consider models with a range of  $S^+/S$  here. We adopt the solar photospheric abundances of Asplund et al. (2009):  $N/H = 6.8 \times 10^{-5}$ ,  $S/H = 1.3 \times 10^{-5}$ , and  $O/H = 4.9 \times 10^{-4}$ . We assume that the emission from different atomic species arises co-spatially, and that the temperature, ionization, and abundances do not vary significantly along a given line of sight.

Given these assumptions, we compare the observed and expected emission-line ratios for a range of  $T_4$  and  $S^+/S$ . In the top panel of Fig. 3, we plot  $[\text{NII}]\lambda 6583/\text{H}\alpha$  vs.  $[\text{SII}]\lambda 6717/\text{H}\alpha$  observed along the minor axis in s1. We also show the median and median absolute deviation of these line ratios observed in s2; these ratios do not show a strong trend with slit position at this location. Both line ratios clearly increase as a function of  $z$ , a trend commonly observed in the eDIG of edge-on galaxies and often interpreted as evidence of increasing  $T_4$  with  $z$  (e.g., Haffner et al. 1999). At  $|z| > 2$  kpc, the line ratios suggest a temperature of  $T_4 = 0.8 - 1.0$  and an ionization fraction of  $S^+/S \sim 0.5 - 0.75$ . There is also a trend toward increasing  $S^+/S$  with  $z$  as  $S^{++}$  becomes  $S^+$  in a more dilute radiation field.

In the bottom panel of Fig. 3, we plot  $[\text{NII}]\lambda 6583/\text{H}\alpha$  vs.  $[\text{OII}]\lambda 3727/\text{H}\alpha$  observed along the filament in s3. Since the  $[\text{OII}]$  doublet is not resolved in these observations, the  $[\text{OII}]$  intensity is integrated over both lines. As  $N^+/N$  and  $O^+/O$  are thought to be comparable in the DIG, these line ratios depend only on temperature for fixed abundances. We compare the observed and predicted line ratios for a range of temperatures, and we find that the observed ratios fall at lower values of  $[\text{OII}]\lambda 3727/\text{H}\alpha$  than expected for a given value of  $[\text{NII}]\lambda 6583/\text{H}\alpha$ . This may be due to selective internal extinction reddening the  $[\text{OII}]\lambda 3727/\text{H}\alpha$  line ratios within the dusty, thick-disk ISM. Additionally, both line ratios

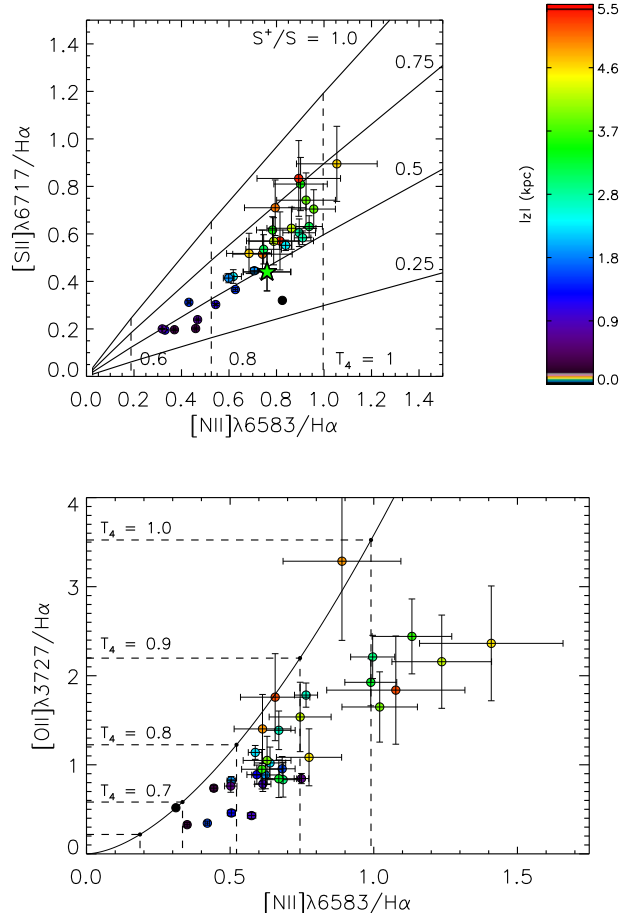


FIG. 3.— Top:  $[\text{NII}]\lambda 6583/\text{H}\alpha$  vs.  $[\text{SII}]\lambda 6717/\text{H}\alpha$  color-coded by  $|z|$  along the minor axis (s1). The median and median absolute deviation of the line ratios from s2 are shown by the star and accompanying error bar. The solid lines indicate the expected line ratios for a range of  $T_4$  at fixed  $S^+/S$ . The dashed lines mark locations of constant  $T_4$ . The rising line ratios suggest an increase in  $T_4$  with  $|z|$ . Bottom:  $[\text{NII}]\lambda 6583/\text{H}\alpha$  vs.  $[\text{OII}]\lambda 3727/\text{H}\alpha$  color-coded by  $|z|$  along the filament studied in s3. The observed line ratios generally fall below the predicted ratios at all  $T_4$ , likely due to selective internal extinction and/or abundance effects. As in the top panel, these results suggest increasing  $T_4$  with  $|z|$  and an eDIG temperature of  $0.8 \leq T_4 \leq 1.0$ .

may be affected by underlying stellar absorption that reduces the measured H $\alpha$  intensity. However, it is not clear that the observed and expected line ratios converge at large  $z$  where these effects are likely minimal. Thus, it is possible that enhancement in the  $N$  abundance with respect to  $O$  is also responsible.

From Fig. 3, we adopt an eDIG temperature of  $T_4 = 0.9$  for the rest of this paper. As we will see in §3.3.2, the turbulent velocity dispersion far exceeds the

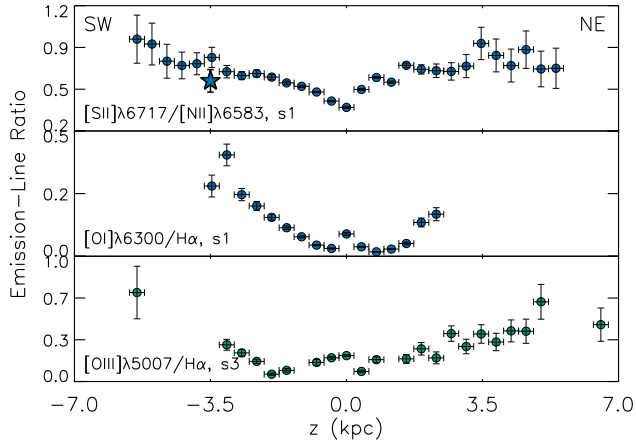


FIG. 4.—  $[\text{SII}]\lambda 6717/[\text{NII}]\lambda 6583$  (top; s1),  $[\text{OI}]\lambda 6300/\text{H}\alpha$  (middle; s1), and  $[\text{OIII}]\lambda 5007/\text{H}\alpha$  (bottom; s3) as functions of  $z$ . The observed increase in  $[\text{OI}]/\text{H}\alpha$  and  $[\text{OIII}]/\text{H}\alpha$  suggests a supplemental heating and/or ionization source such as shocks or turbulent mixing layers (Collins & Rand 2001).

thermal velocity dispersion, and thus uncertainty in the eDIG temperature on the order of 10–20% is unimportant for our dynamical equilibrium study. Out of the disk, the observed  $[\text{SII}]\lambda 6717/[\text{SII}]\lambda 6731 \sim 1.5$  in s1 and  $[\text{OII}]\lambda 3729/[\text{OII}]\lambda 3726 \sim 1.5$  in s3uv demonstrate that the eDIG is in the low-density limit as expected (e.g., Osterbrock & Ferland 2006).

The emission-line ratios of eDIG layers are also of interest due to the challenge that they present to photoionization models (e.g., Collins & Rand 2001). We comment briefly on that here. In Fig. 4, we show  $[\text{SII}]\lambda 6717/[\text{NII}]\lambda 6583$  and  $[\text{OI}]\lambda 6300/\text{H}\alpha$  as functions of  $z$  along the minor axis (s1) and  $[\text{OIII}]\lambda 5007/\text{H}\alpha$  as a function of  $z$  in s3. (Note that detection of the  $[\text{OI}]$  line in s3 is impeded by sky-line residuals. We also choose to take the ratio of  $[\text{OIII}]$  to  $\text{H}\alpha$  instead of the more traditional  $\text{H}\beta$  because the latter is not detected at large  $z$  and is contaminated by the underlying stellar absorption line at low  $z$ .)

In a photoionization model, we expect  $[\text{SII}]\lambda 6717/[\text{NII}]\lambda 6583$  to increase with distance from the ionizing source as  $S^{++} \rightarrow S^+$ . We do observe an increase in  $[\text{SII}]/[\text{NII}]$  as a function of  $z$ . However, the rise in  $[\text{OIII}]\lambda 5007/\text{H}\alpha$  with  $z$  is associated with a need for an additional source of heating and/or ionization, such as shocks or turbulent mixing layers (e.g., Collins & Rand 2001). The presence of shocks is further suggested by the rising  $[\text{OI}]\lambda 6300/\text{H}\alpha$ . Since the neutral fractions of O and H are coupled via charge exchange, the presence of  $[\text{OI}]$  emission suggests a multiphase medium, as is found in shock-compressed regions (e.g., Collins & Rand 2001). The need for an additional source of heating and/or ionization that behaves differently than photoionization will be relevant as we consider the dynamical state of the eDIG layer in Sections §4 and §5.

From Fig. 4, we can also verify the validity of our assumption that  $N^+/N$  is high by confirming that  $N^{++}/N$  must be low. Due to the similarly high second ionization potentials of O and N, a low  $O^{++}/O$  suggests a similarly low  $N^{++}/N$ . Our observed  $[\text{OIII}]\lambda 5007/\text{H}\alpha$  line ratios and the electron temperature deduced from Fig. 3

( $T_e = 0.9$ ) imply a median value of  $O^{++}/O = 0.1$ , confirming a low value of  $N^{++}/N$ . (We thank R. Rand for this suggestion.)

### 3.3. eDIG Kinematics

#### 3.3.1. Radial Velocities

The heliocentric, line-of-sight  $\text{H}\alpha$  velocity,  $v_{\text{H}\alpha}$ , observed in s2 is shown in Fig. 5. The  $\text{H}\alpha$  rotation curve at  $z = -3.5$  kpc is compared to a model of the HI rotation curve at  $z = 0$  kpc from Irwin (1994). West and east of the minor axis,  $v_{\text{H}\alpha}$  is closer to the systemic velocity than  $v_{\text{HI}}$  by a median  $\Delta v = 71 \text{ km s}^{-1}$  and  $\Delta v = 54 \text{ km s}^{-1}$  at  $|R| \geq 3$  kpc, respectively. The eDIG layer thus shows the signature of a lagging gaseous halo that arises as a consequence of the conservation of angular momentum in a disk-halo flow. The larger asymmetric drift of the warmer gas may also contribute to the velocity discrepancy between the two phases.

If the line-of-sight velocity samples gas at the tangent point and is thus a measure of the rotational velocity, then this implies a rotational velocity gradient of  $\Delta v = -20.3 \text{ km s}^{-1} \text{ kpc}^{-1}$  and  $\Delta v = -15.4 \text{ km s}^{-1} \text{ kpc}^{-1}$  for positive and negative  $R$ , respectively. However, this is significantly steeper than the  $-1 \text{ km s}^{-1} \text{ arcsec}^{-1}$  ( $-7 \text{ km s}^{-1} \text{ kpc}^{-1}$ ) determined by Heald et al. (2006) for this galaxy. These authors demonstrate that quantification of the true rotational velocity gradient is dependent on robust modeling of a three-dimensional, rotating disk in which the density distribution and rotation curve are allowed to vary with distance from the midplane. Thus, we avoid over-interpreting the relatively steep velocity gradients observed here, as they may be biased by local filamentary structure and may not reflect the true rotational velocity of the eDIG layer.

The top panel of Fig. 6 shows  $v_{\text{H}\alpha}$  as a function of  $z$  observed on the minor axis in s1. There is a spread in  $v_{\text{H}\alpha}$  at small  $z$  before it approaches  $v_{\text{sys}}$  at larger  $z$ . At the largest  $z$ ,  $v_{\text{H}\alpha}$  is blueshifted with respect to  $v_{\text{sys}}$ , moving away from the systemic velocity at increasing distances from the midplane. If the eDIG layer is cylindrically rotating, then we would expect  $v_{\text{H}\alpha} \sim v_{\text{sys}}$  along the minor axis. Although the spread in  $v_{\text{H}\alpha}$  at small  $z$  is likely due to the deviation of the inclination angle from  $i = 90^\circ$ , the blueshifted velocities observed at large  $z$  merit further discussion in §5.

The bottom panel of Fig. 6 again shows  $v_{\text{H}\alpha}$  as a function of  $z$ , here observed perpendicular to the disk at  $R = 6.5$  kpc in s3. As previously found at this location by Rand (2000),  $v_{\text{H}\alpha}$  climbs steadily from the rotational velocity in the disk,  $v_{\text{disk}} \sim 1550 \text{ km s}^{-1}$ , to the systemic velocity,  $v_{\text{sys}} = 1681 \text{ km s}^{-1}$ , as  $z$  increases ( $v_{\text{sys}}$  is derived using the optical convention from the HI redshift of de Vaucouleurs et al. 1991).  $v_{\text{H}\alpha}$  reaches  $v_{\text{sys}}$  around  $z = 5$  kpc, displaying small variations around the systemic velocity at larger  $z$ . A similar trend is seen on the southwest side of the galaxy, although  $v_{\text{H}\alpha}$  approaches  $v_{\text{sys}}$  at a slower rate and does not reach  $v_{\text{sys}}$  over the spatial extent of our emission-line detections. Within  $|z| \leq 5$  kpc, the velocity gradients are approximately  $\Delta v \sim -25 \text{ km s}^{-1} \text{ kpc}^{-1}$  and  $\Delta v \sim -6 \text{ km s}^{-1} \text{ kpc}^{-1}$  on the northeast and southwest sides, respectively. While this is consistent with the presence of a rotational velocity gradient, we again caution against quantifying this

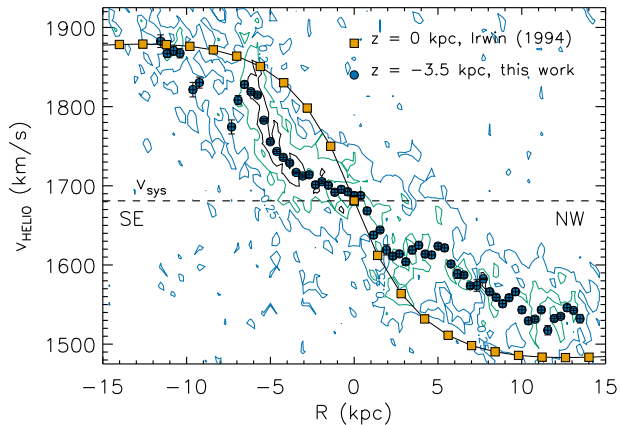


FIG. 5.— Line-of-sight, heliocentric  $H\alpha$  velocities as a function of  $R$  observed in s2 ( $z = -3.5$  kpc; blue) compared to a model HI rotation curve from Irwin (1994) ( $z = 0$  kpc; yellow). The blue, green, and black contours illustrate the position-velocity diagram at 25%, 50%, and 75% of the maximum  $H\alpha$  intensity, respectively. The tendency of the eDIG layer towards systemic velocity is characteristic of lagging gaseous halos; we find median velocity offsets of  $\Delta v = -20.3$   $\text{km s}^{-1} \text{kpc}^{-1}$  and  $\Delta v = -15.4$   $\text{km s}^{-1} \text{kpc}^{-1}$  west and east of the minor axis, respectively.

gradient without additional modeling.

It is interesting to ask whether there is any evidence of perturbations to the line-of-sight velocities due to the interaction with NGC 5774. The most likely place to find such evidence would be in s2 where the slit extends across the HI bridge between the galaxies. However, we only detect emission to  $R = 13.5$  kpc on this side of the galaxy, suggesting that any ionized gas in the bridge has too low surface brightness to be detected here. The blueshifted velocities at large  $z$  on the minor axis are the subject of further discussion in §5, including their possible relationship to an interaction.

### 3.3.2. Turbulent Velocity Dispersion

The  $H\alpha$  emission-line widths,  $\sigma_{H\alpha}$ , are shown as a function of  $z$  along the minor axis in Fig. 7. These line widths refer to the standard deviation of the Gaussian velocity distribution. In the disk, where we expect  $\sigma_{H\alpha}$  to be characteristic of HII regions ( $\sigma_{HII} \sim 20$   $\text{km/s}$ ), the line width is limited by the spectral resolution ( $\sigma_{res} \sim 26$   $\text{km s}^{-1}$ ). However,  $\sigma_{H\alpha}$  smoothly increases with  $z$ , reaching values as high as  $\sim 70$   $\text{km s}^{-1}$  by  $|z| = 5$  kpc. The median and median absolute deviation observed in s2 ( $z = -3.5$  kpc) is  $\sigma_{H\alpha} = 58 \pm 11$   $\text{km s}^{-1}$ ; there is no obvious trend in  $\sigma_{H\alpha}$  with  $R$ .

This is the first clear evidence of an increase in emission-line widths as a function of height above the disk in an eDIG layer. The line widths appear to rise within  $|z| \leq 4$  kpc and then plateau at some characteristic value. As discussed in §3.1, the impact of dust extinction on the observed velocity dispersion is likely to be small, as the increase in  $\sigma_{H\alpha}$  with  $z$  is observed at several dust scale heights above the disk. Several factors contribute to the line width, including thermal, turbulent, and noncircular motions (note that we have already corrected for the spectral resolution, and rotational motions are minimized on the minor axis). The thermal line width of a gas with  $T_4 \sim 0.9$  is small compared to the

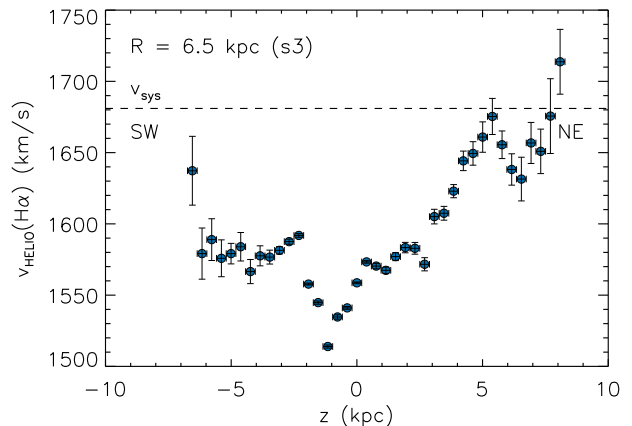
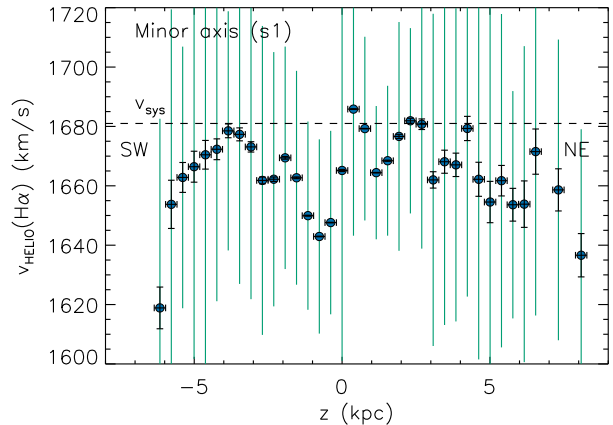


FIG. 6.— Line-of-sight, heliocentric  $H\alpha$  velocities as a function of  $z$  observed on the minor axis (top; s1) and at  $R = 6.5$  kpc (bottom; s3). At top, the green bars indicate the emission-line widths,  $\sigma_{H\alpha}$  (see §3.3.2). At bottom, the observed velocity gradients of  $\Delta v \sim -25$   $\text{km s}^{-1} \text{kpc}^{-1}$  (northeast) and  $\Delta v \sim -6$   $\text{km s}^{-1} \text{kpc}^{-1}$  (southwest) are consistent with a previously-observed lagging halo (e.g., Rand 2000; Heald et al. 2006), though we do not attempt to quantify the rotational velocity gradient here.

observed line widths ( $\sigma_{th} \sim 10$   $\text{km s}^{-1}$ ); in the absence of information about contributions from noncircular motions, we take the observed line widths as an upper limit on the turbulent velocity dispersion in the eDIG layer. Here, “turbulence” refers to any random gas motions, including the cloud-cloud velocity dispersion. We discuss possible origins for the  $z$ -dependence of  $\sigma_{H\alpha}$  in §5.

## 4. A DYNAMICAL EQUILIBRIUM MODEL

We now ask whether the eDIG layer in NGC 5775 is well-represented by a dynamical equilibrium model - that is, whether the thermal, turbulent, magnetic field, and cosmic-ray pressure gradients are sufficient to satisfy the equation of hydrostatic equilibrium. (We favor the term “dynamical equilibrium” over “hydrostatic equilibrium” due to the inclusion of turbulent motions in the relevant sources of pressure support.) We follow the approach described in Boettcher et al. (2016), which we summarize here.

We solve the hydrostatic equilibrium equation for an

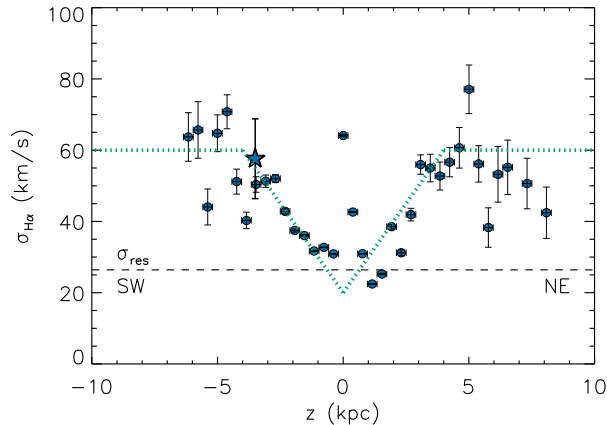


FIG. 7.—  $H\alpha$  line widths,  $\sigma_{H\alpha}$ , as a function of  $z$  on the minor axis (s1), where contributions from rotational velocity are minimized.  $\sigma_{H\alpha}$  is corrected for the spectral resolution, indicated by the dashed black line. The median and median absolute deviation from s2 are shown by the star and accompanying error bar.  $\sigma_{H\alpha}$  displays an increase with  $z$  within several kiloparsecs of the disk, the first clear detection of such a trend in an eDIG layer. The dotted green line shows the functional form of  $\sigma(z)$  used in §4.

eDIG layer in pressure balance given by:

$$\frac{dP(z, R)}{dz} = -\frac{d\Phi(z, R)}{dz}\rho(z, R). \quad (8)$$

Here,  $P(z, R)$  and  $\rho(z, R)$  are the gas pressure and density, respectively, and  $\frac{d\Phi(z, R)}{dz} = g_z(z, R)$  is the gravitational acceleration derived from the galactic gravitational potential,  $\Phi(z, R)$ . We discuss the mass model used to determine the galactic gravitational potential in the Appendix.

We consider contributions from gas pressure,  $P_g$ , magnetic field pressure,  $P_B$ , and cosmic-ray pressure,  $P_{cr}$  (note that we do not consider magnetic tension):

$$P(z, R) = P_g + P_B + P_{cr}. \quad (9)$$

The gas pressure is dependent on the velocity dispersion,  $\sigma$ , that in turn depends on both thermal ( $\sigma_{th}$ ) and turbulent ( $\sigma_{turb}$ ) motions:

$$P_g(z, R) = \sigma(z)^2\rho(z, R), \sigma(z)^2 = \sigma_{th}^2 + \sigma_{turb}^2. \quad (10)$$

Our goal is to determine whether we can satisfy Eq. (8) given the observed gas density distribution,  $\rho(z)$ , and the observed pressure gradients,  $\frac{dP}{dz} = \frac{dP_g}{dz} + \frac{dP_B}{dz} + \frac{dP_{cr}}{dz}$ . In §4.1 - §4.4 below, we derive expressions for the relevant pressure gradients, expressed for a single component of the density distribution. As the pressure gradients are derived from observations integrated across the disk, we assume that only the gravitational acceleration has radial dependence. Thus, we take these gradients as representative of the average vertical pressure support in the eDIG layer. The lack of significant variation in the observed emission-line widths as a function of projected galactocentric radius in s2 supports this approach; note, however, that the line widths can be broadened by integration through a rotating medium away from the minor axis.

#### 4.1. Thermal Pressure Gradient

From Eq. (10), the thermal gas pressure is given by  $P_{th}(z) = \sigma_{th}^2\rho(z)$ , where the thermal velocity dispersion can be expressed as  $\sigma_{th} = \sqrt{\frac{kT}{\alpha m_p}}$ . Here,  $k$  is the Boltzmann constant,  $m_p$  is the proton mass, and  $\alpha$  is a scaling factor. We take  $\alpha = 0.62$  assuming that the gas is 9% He by number, with 100% and 70% of the H and He ionized, respectively (Rand 1997, 1998). For a gas with  $T_4 = 0.9$  (§3.2), we find  $\sigma_{th} = 11 \text{ km s}^{-1}$ . Assuming that  $\sigma_{th}$  does not change substantially with  $z$ , then the thermal pressure gradient is given by:

$$\frac{dP_{th}}{dz} = -\frac{\sigma_{th}^2}{h_z}\rho(z). \quad (11)$$

#### 4.2. Turbulent Pressure Gradient

Like the thermal gas pressure, the turbulent gas pressure is given by  $P_{turb}(z) = \sigma_{turb}(z)^2\rho(z)$ , except here we allow the velocity dispersion to vary with  $z$ . By eye, we fit the following functional form to  $\sigma_{turb}(z)$ , assuming isotropic turbulence (see the green dotted line in Fig. 7):

$$\sigma_{turb}(z) = \begin{cases} \sigma_0 + m_\sigma z, & \text{if } 0 \text{ kpc} \leq |z| \leq 4 \text{ kpc} \\ \sigma_1, & \text{if } |z| > 4 \text{ kpc}. \end{cases} \quad (12)$$

Here, we use  $\sigma_0 = 20 \text{ km s}^{-1}$ ,  $m_\sigma = 10 \text{ km s}^{-1}\text{kpc}^{-1}$ , and  $\sigma_1 = 60 \text{ km s}^{-1}$ .

Note again that the observed  $\sigma(z)$  is an upper limit to the true  $\sigma_{turb}(z)$  due to possible contributions from non-circular motions. We have also not corrected the observations for the (small) contribution from thermal motions. This yields the following turbulent pressure gradient:

$$\frac{dP_{turb}}{dz} = \begin{cases} 2m_\sigma\sigma_{turb}(z)\rho(z) - \frac{\sigma_{turb}(z)^2}{h_z}\rho(z), & \text{if } 0 \text{ kpc} \leq |z| \leq 4 \text{ kpc} \\ -\frac{\sigma_1^2}{h_z}\rho(z), & \text{if } |z| > 4 \text{ kpc}. \end{cases} \quad (13)$$

#### 4.3. Magnetic Pressure Gradient

To estimate the magnetic field and cosmic-ray pressure gradients, we turn to the radio continuum observations discussed in §1. Krause et al. (2018) characterize the magnetic field strengths in the disks and the synchrotron scale heights of galaxies in the CHANG-ES sample, including thin disk and halo components. For NGC 5775, they find a disk field strength of  $B_0 = 14.8 \mu\text{G}$  and halo synchrotron scale heights of  $h_{z, syn} = 1.46 \pm 0.13 \text{ kpc}$  (C-band D-array; centered at 6 GHz) and  $h_{z, syn} = 1.98 \pm 0.35 \text{ kpc}$  (L-band C-array; centered at 1.5 GHz). We discuss the thin synchrotron disk in §5.

To estimate the magnetic pressure gradient in the halo of NGC 5775, we assume energy equipartition between the magnetic field and cosmic-ray energy densities (see §5 for a discussion of the merits of this assumption). Under this assumption, the synchrotron scale height is related to the magnetic field scale height via the nonthermal spectral index:  $h_{z, B} \sim h_{z, syn}(3 + \alpha)$  (Beck 2015). Note that  $h_{z, B}$  may be even larger due to energy losses of cosmic-ray electrons lowering the synchrotron scale height.

For  $\alpha = 1.09$  (Krause et al. 2018),  $h_{z, B} = 6 \text{ kpc}$  and  $h_{z, B} = 8.1 \text{ kpc}$  determined from the 6 GHz and 1.5 GHz observations, respectively. We adopt the latter value here, as lower frequency emission arises from lower energy cosmic rays that undergo fewer losses than their

higher energy counterparts. The vertical distribution of lower energy cosmic-ray electrons therefore better approximates the distribution of (lossless) cosmic-ray protons; the cosmic-ray pressure, of interest in §4.4, arises from this latter component.

We assume a simple, plane-parallel geometry for the halo component of the magnetic field, where:

$$B(z) = B_0 e^{-|z|/h_{z,B}}. \quad (14)$$

Therefore, given  $P_B = \frac{B(z)^2}{8\pi}$ , the magnetic pressure gradient can be written as:

$$\frac{dP_B(z)}{dz} = -\frac{2}{h_B} P_B. \quad (15)$$

The observed ‘‘X-shaped’’ morphology of the halo magnetic field suggests that it becomes increasingly vertical at large  $z$  (Soida et al. 2011). However, the likely presence of a significant turbulent component to the field mitigates the effect of the field geometry on the magnetic pressure gradient.

#### 4.4. Cosmic-ray Pressure Gradient

To determine the cosmic-ray pressure gradient, we again assume equipartition between the magnetic field and cosmic-ray energy densities. Since the majority of the cosmic-ray energy density is believed to be due to only mildly relativistic protons (Ferrière 2001), we take  $P_{cr} = 0.45U_{cr} = 0.45U_B$  and find:

$$\frac{dP_{cr}(z)}{dz} = 0.45 \frac{dP_B(z)}{dz}. \quad (16)$$

#### 4.5. Testing Dynamical Equilibrium

We first test the dynamical equilibrium model for an initial choice of parameters: a volume filling factor of  $\phi = 1$  (no gas clumping) and the magnetic field properties discussed in §4.3. We restrict our analysis to  $|z| \geq 1$  kpc, as the nature of the gas density profile within  $|z| < 1$  kpc is not well characterized due to obscuration by dust and HII regions and the slight inclination of the disk from edge-on. We thus assume that some boundary condition governs the meeting of the eDIG layer with the thin-disk ISM at small  $z$ . We analyze each side of the galaxy individually, assessing the dynamical state of the thick disk and halo both together and separately.

We calculate the thermal, turbulent, magnetic field, and cosmic-ray pressure gradients and compare the total observed gradient with the required gradient (in other words, with the right-hand side of Eq. 8). We consider the model satisfied if the observed pressure support equals or exceeds the required support at  $|z| \geq 1$  kpc. We do so at every galactocentric radius between the center and the edge of the eDIG layer ( $0 \text{ kpc} \leq R \leq 14 \text{ kpc}$ , in steps of  $\Delta R = 1 \text{ kpc}$ ), and we determine the minimum radius at which the dynamical equilibrium model is satisfied,  $R_{eq}$ .

In Fig. 8, we present the observed and required pressure gradients at  $R_{eq}$  for each side of the galaxy and each eDIG component considered. The halo components are most easily supported in dynamical equilibrium, with  $R_{eq} = 8 \text{ kpc}$  ( $R_{eq} = 9 \text{ kpc}$ ) on the northeast (southwest) sides of the galaxy. Both thick disk components have a similar result ( $R_{eq} = 9 \text{ kpc}$ ). Combining the components

renders the model more difficult to satisfy, pushing  $R_{eq}$  to  $R_{eq} = 10 \text{ kpc}$  on the northeast side and to  $R_{eq} = 11 \text{ kpc}$  on the southwest side.

It is clear that there is insufficient vertical pressure support to satisfy dynamical equilibrium except in the shallowest parts of the galactic gravitational potential. In other words,  $R_{eq}$  is a significant fraction of the radial extent of the eDIG layer for all components considered. The success of such a model thus requires placing the gas in a ring geometry at moderate to large  $R$ , perhaps over star-forming spiral arms. It is the magnetic pressure gradient, followed by the cosmic-ray pressure gradient, that provides the most substantial source of vertical support.

Note that there is a discontinuity in  $\frac{dP_{turb}}{dz}$  at  $|z| = 4$  kpc, where the turbulent velocity dispersion transitions from a rising to a flat regime. This discontinuity is most prominent in the halo component. At  $|z| \leq 4$  kpc,  $\frac{dP_{turb}}{dz}$  is positive; this is because  $\sigma(z)^2$  rises more quickly than  $\rho(z)$  falls due to the large scale height of the halo. At  $|z| > 4$  kpc,  $\frac{dP_{turb}}{dz}$  becomes negative as  $\sigma(z)^2$  becomes constant and  $\rho(z)$  continues to fall. The total pressure gradient remains negative at all  $z$  due to contributions from the magnetic field and cosmic rays.

From Eq. (8), a discontinuity in  $\frac{dP}{dz}$  implies a jump in  $\rho(z)$  (in this case, an increase in  $\rho(z)$  at  $|z| = 4$  kpc). This is an unstable configuration. Thus, we interpret the total observed pressure gradients in Fig. 8 not as the true pressure gradients that we seek to reproduce with a density model, but instead as an indication of the maximum available pressure support in the eDIG layer. This allows us to assess the viability of the dynamical equilibrium model without claiming a precise characterization of the true pressure profile. We also note that the turbulent motions in the halo component may differ from those in the thick disk; since the latter dominate the line profiles, we do not wish to overinterpret  $\frac{dP_{turb}}{dz}$  in the halo.

We now explore how variations in  $\phi$ ,  $B_0$ , and  $h_{z,B}$  affect the success of the dynamical equilibrium model. We vary  $\phi$  from 0.01 (highly clumpy) to 1 (no clumping) and  $B_0$  and  $h_{z,B}$  both by 50% ( $7.4 \mu\text{G} \leq B_0 \leq 22.2 \mu\text{G}$ ,  $4.05 \text{ kpc} \leq h_{z,B} \leq 12.15 \text{ kpc}$ ). Within this parameter space, we conduct the analysis described above for the thick disk and halo combined and determine the value of  $R_{eq}$ .

We show results in this parameter space in Fig. 9 for the northeast (top) and southwest (bottom) sides of the galaxy. In the top two panels for each side, we display  $R_{eq}$  in the  $\phi$ ,  $B_0$  ( $h_{z,B} = 8.1 \text{ kpc}$ ) and  $\phi$ ,  $h_{z,B}$  ( $B_0 = 14.8 \mu\text{G}$ ) planes. Everywhere in these panels,  $R_{eq} \geq 7 \text{ kpc}$ ; this confirms the need for a ring geometry for the dynamical equilibrium model to succeed.

In general, for the gas to be supported at a given galactocentric radius, a higher magnetic field strength (a steeper  $\frac{dP_B}{dz}$ ) is required for a smaller  $\phi$  (a steeper  $\frac{d\rho}{dz}$ ). Likewise, a smaller  $h_{z,B}$  (a steeper  $\frac{dP_B}{dz}$ ) is needed to support the gas given a smaller  $\phi$ . As the eDIG scale height begins to exceed the magnetic scale height, it is more difficult to support the eDIG at  $|z| > h_{z,B}$ , and larger values of  $\phi$  are again required.

We briefly consider the impact of a radially-dependent eDIG density distribution on the success of the dynamical

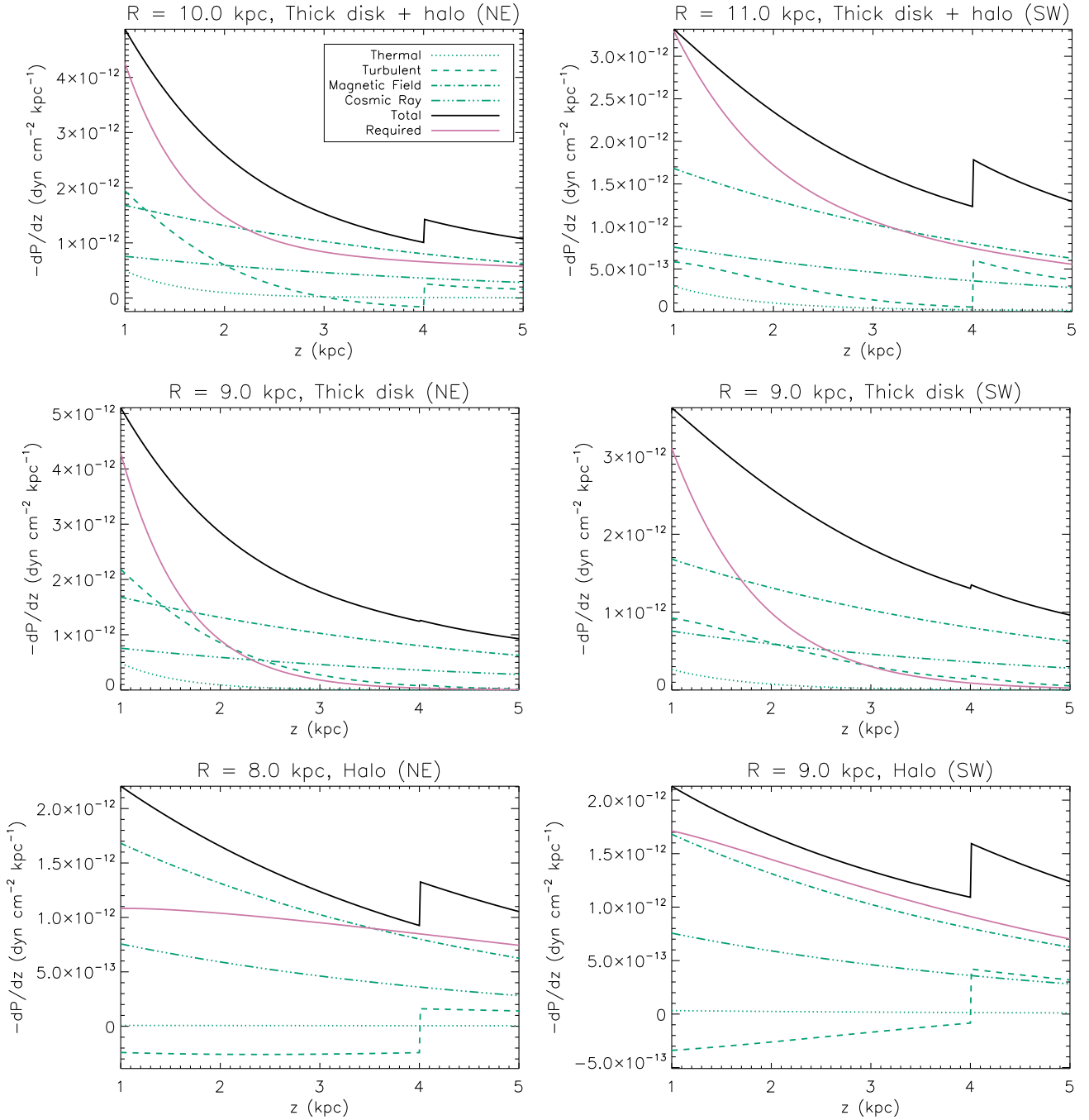


FIG. 8.— Comparison of observed (black) and required (pink) pressure gradients to satisfy a dynamical equilibrium model for the northeast (left) and southwest (right) sides of the eDIG layer, shown at the *minimum* galactocentric radii at which the dynamical equilibrium model is satisfied. At all smaller galactocentric radii, the required pressure gradient exceeds the observed gradient, and the model fails. Models with thick disk and halo (top), thick disk (middle), and halo (bottom) components are considered. The magnetic field is the dominant source of vertical pressure support.

cal equilibrium model. For radial dependence of the form  $n_e(R) \propto e^{-R/h_R}$ , a reasonable choice of  $h_R$  (i.e., a few kpc, comparable to the stellar scale length) has only a small effect on the model’s success. For example, a choice of  $h_R = 4$  kpc mildly reduces  $R_{eq}$  to 8 kpc from 10 and 11 kpc for the combined thick disk and halo models on the northeast and southwest sides of the disk, respectively. This minor reduction in  $R_{eq}$  is expected if the gas surface density decreases with  $R$ , rendering the model easier to satisfy at large galactocentric radii. In the absence of a comparable radial dependence in the magnetic field strength, such a radial fall-off in the density distribution produces a magnetic pressure comparable to the gas pressure (thermal and turbulent) at small  $R$ , but in excess of the gas pressure by an order of magnitude at  $R = 10$  kpc. In a model lacking radial dependence, the magnetic pressure exceeds the gas pressure by a factor of  $\sim 2$ , more consistent with approximate energy equipartition.

#### 4.6. Stability Analysis

The magnetic buoyancy instability first described by Parker (1966) presents another challenge to the success of our dynamical equilibrium model. Although Parker considered cosmic rays as a fluid with an adiabatic index  $\gamma_{cr} = 0$ , we allow for cosmic ray coupling to the gas either via extrinsic turbulence or via the streaming instability for high and low energy cosmic rays, respectively ( $\gamma_{cr} = 1.45$  given  $P_{cr} = 0.45U_{cr}$ ; Zweibel 2013). This allows the cosmic rays to act toward stabilizing the gas as well as elevating it above its natural scale height.

These considerations yield the following stability criterion (Newcomb 1961; Parker 1966; Zweibel & Kulsrud 1975):

$$-\frac{d\rho}{dz} > \frac{\rho^2 g_z}{\gamma_g P_g + \gamma_{cr} P_{cr}}. \quad (17)$$

To determine whether the eDIG layer is robust against the instability, we calculate the minimum value of  $\gamma_g$  required to satisfy this criterion for both  $\gamma_{cr} = 0$  (no cosmic ray coupling) and  $\gamma_{cr} = 1.45$  (cosmic ray coupling). An adiabatic index of  $\gamma_g = 5/3 - 2$  may be characteristic of the star-forming, turbulent ISM (Zweibel & Kulsrud 1975); however, values as low as  $\gamma_g = 1$  may be found in the eDIG (Parker 1966). Therefore, we define a stable model as that for which the minimum value of  $\gamma_g$  that satisfies the stability criterion is  $\gamma_g \leq 1$ .

Heintz & Zweibel (2018) have recently demonstrated the potential importance of cosmic-ray streaming to the stability of the magnetized ISM. They illustrate that inclusion of cosmic-ray streaming can be destabilizing due to cosmic-ray heating. This effect is mitigated in the isothermal case ( $\gamma_g = 1$ ). Future work will explore the implementation of cooling and the characteristic wavelength of the instability in the nonlinear regime, potentially shedding light on the impact, if any, of cosmic-ray heating on the electron temperature and/or ionization structure of the eDIG. However, it is important to note that even if a model satisfies the stability criterion above, the model may be unstable if heating via cosmic-ray streaming is important.

We perform the stability analysis between  $1 \text{ kpc} \leq |z| \leq 10 \text{ kpc}$ . It is important to note that our treatment

of the instability is based on a one-dimensional model and may fail at large  $z$ . In Fig. 10, we present the minimum values of  $\gamma_g$  required to satisfy the stability criterion for the thick disk and the halo, separately and combined. Models with  $\gamma_{cr} = 0$  are not stable at all  $z$  for the relevant  $R$ ; thus, it is clear that the cosmic rays must be coupled to the gas to achieve a stable model.

Allowing  $\gamma_{cr} = 1.45$ , the thick disk is stable at all radii at which the dynamical equilibrium model succeeds. In contrast, the halo on the northeast (southwest) side of the disk is not stable at all  $z$  until  $R > 14$  kpc ( $R \geq 10$  kpc). The instability of the halo is exacerbated by the large scale height on the northeast side. A gas cloud perturbed upwards will be buoyant if the rate at which its internal density decreases is faster than the rate at which the background density decreases. This is more likely to occur in a medium in which the gas density profile changes only slowly, rendering the halo less stable than the thick disk. While the coupled cosmic rays can “stiffen” the equation of state of the medium and thus decrease the minimum galactocentric radius at which a stable model can be achieved, this effect is insufficient to produce stable models outside of a thin ring, or at all, on the southwest and northeast sides of the disk, respectively.

We now consider the effect of stability on the parameter space study discussed in the previous section. We ask where in parameter space a *stable*, successful dynamical equilibrium model is found, and show the results in Fig. 9. For the northeast side of the disk,  $R_{eq}$  increases to  $R_{eq} \geq 14$  kpc as compared to  $R_{eq} \geq 7$  kpc in the slices of parameter space previously considered; this is due to the instability of the halo at large  $z$  seen in Fig. 10. On the southwest side of the disk, for which the halo scale height is a factor of  $\sim 2$  smaller than on the northeast side, the areas of parameter space over which the dynamical equilibrium model succeeds and over which it succeeds *and* is stable are much more comparable. The instability of the dynamical equilibrium model at almost all galactocentric radii on the northeast side effectively rules out this model for this side of the galaxy.

## 5. DISCUSSION

Comparing the results of Boettcher et al. (2016) to those presented here, a dynamical equilibrium model fails in a similar way for the eDIG layers in the Milky-Way analog NGC 891 and the interacting, star-forming galaxy NGC 5775. In both systems, stably supporting the eDIG layer in dynamical equilibrium is only feasible at moderate to large galactocentric radii, requiring a contrived ring geometry that is inconsistent with observations of face-on disk galaxies (e.g., Boettcher et al. 2017). Such a model relies predominantly on the magnetic field and cosmic ray pressure gradients to support the eDIG layers at their observed scale heights.

Although the great vertical extent of the eDIG layer in NGC 5775 may follow from its enhanced star-formation rate per unit area, factor(s) other than the star-formation rate surface density set the vertical extents of the synchrotron halos in the CHANG-ES sample analyzed by Krause et al. (2018). In this sample, the synchrotron scale heights are positively correlated with the synchrotron diameters of the galaxies. Although more work is needed to interpret this trend in the context of eDIG

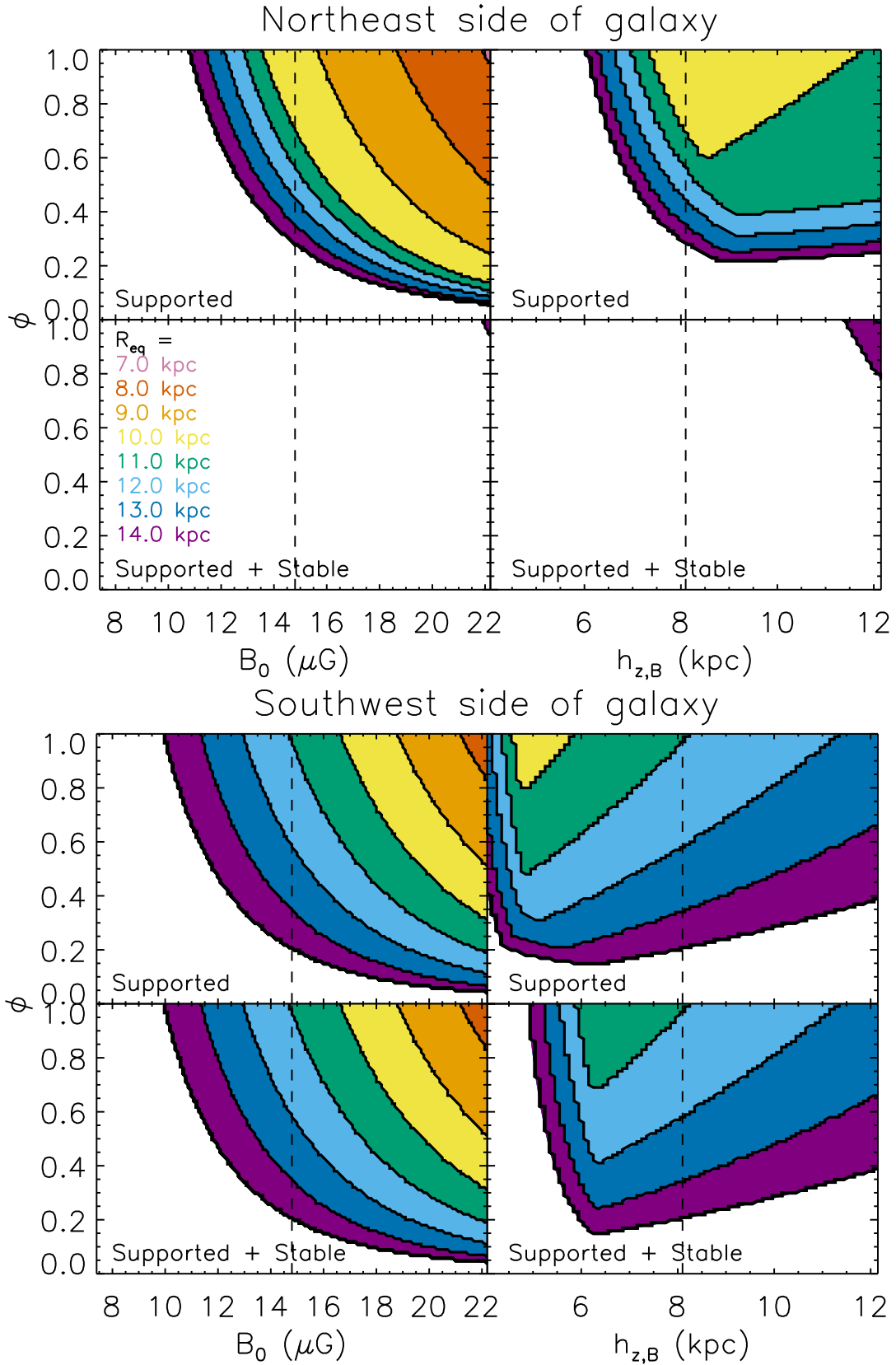


FIG. 9.— Exploration of the success of a dynamical equilibrium model for the eDIG layer over a range of  $\phi$ ,  $B_0$ , and  $h_{z,B}$ . Both the thick disk and halo components of the eDIG layer are included in the model for the northeast (top) and southwest (bottom) sides of the galaxy. We plot the minimum galactocentric radius at which the dynamical equilibrium model succeeds,  $R_{eq}$ , in the top panels of both figures (labeled “Supported”). We also require the stability criterion given in Eq. 17 to be satisfied in the bottom panels (labeled “Supported and Stable”). The large values of  $R_{eq}$  required for a stable, successful dynamical equilibrium model on the northeast side effectively eliminates this model at this location. The dashed lines indicate the preferred values of  $B_0$  and  $h_{z,B}$ . In the lefthand (righthand) column,  $h_{z,B} = 8.1$  kpc ( $B_0 = 14.8 \mu\text{G}$ ).

layers, it appears that the processes that govern the spatial extents and pressure profiles of the thermal and non-thermal halos do not conspire together to achieve an equilibrium configuration at the disk-halo interface.

We note that there are several caveats to the dynamical equilibrium model presented here. First, we assume that the measured horizontal velocity dispersion is equal to the vertical velocity dispersion. If the vertical dispersion exceeds the horizontal dispersion, as suggested by observations of M83 (Boettcher et al. 2017), then we would underestimate the turbulent pressure support here. Additionally, we do not consider the potential roles of magnetic tension (Boulares & Cox 1990), radiation pressure (e.g., Franco et al. 1991), and the hot halo gas in supporting the eDIG layer at its observed scale height.

The role of the hot halo is of particular interest due to the detection of diffuse, spatially-extended, X-ray-emitting gas in the halo of NGC 5775 (Li et al. 2008; Li & Wang 2013). If the warm and hot phases are sufficiently coupled, then the vertical pressure gradient in the hot halo may merit inclusion in the pressure gradients considered here. This is especially true given the likelihood of a large volume filling factor for the hot phase ( $\phi_{hot} \sim 1$ ). Thus, we make a simple estimate of the vertical pressure support provided by the hot halo.

Li et al. (2008) find two temperature components in the hot, diffuse phase, with electron densities of a few  $\times 10^{-3} \text{ cm}^{-3}$  and temperatures of a few  $\times 10^6 \text{ K}$ . This corresponds to a thermal velocity dispersion of  $\sigma \geq 200 \text{ km s}^{-1}$  and thus a thermal scale height of  $h_z \sim 10 \text{ kpc}$  at a galactocentric radius of  $R \sim 5 \text{ kpc}$  in the galactic gravitational potential given in the Appendix. Assuming a hot halo in hydrostatic equilibrium, the vertical thermal pressure gradient in the hot phase is comparable to that in the warm phase. As we saw in Fig. 8, the thermal pressure gradients are small compared to the nonthermal pressure gradients, and thus the hot phase does not appear to substantially improve the performance of the dynamical equilibrium model.

If the hot phase has a scale height considerably less than its thermal scale height, then it may be able to contribute more substantially to the pressure support. This could occur if the hot phase is confined by a magnetic field that is anchored to the disk via the warm medium. The relatively small scale height observed by Li et al. (2008) for the hot phase ( $h_z \sim 1.5 \text{ kpc}$ ) suggests that such a scenario may be appropriate. However, in this case, a warm and hot phase with comparable scale heights in pressure equilibrium can at most double the contribution to the thermal pressure gradient compared to the warm medium alone. As we have seen, this remains insufficient to support the layer, and thus we conclude that the hot phase is not the source of the missing pressure support in a dynamical equilibrium context. Note that in addition to a diffuse background, a superbubble is detected in X-ray emission to distances of  $|z| \sim 10 \text{ kpc}$  on the southern side of the galaxy. An expanding or outflowing hot halo may impart momentum to the eDIG and thus enhance its scale height, but we consider this as a separate class of models than the hydrostatic case tested here.

Additional assumptions may have affected the success of the dynamical equilibrium model. We employ a simple, plane-parallel magnetic field geometry despite evi-

dence that the field becomes X-shaped at large distances from the midplane (Soida et al. 2011). An increasingly vertical component of the magnetic field with height above the disk introduces the possibility that magnetic tension plays a role in supporting the gas, an effect that appears important in the Galaxy (Boulares & Cox 1990). The presence of a thin synchrotron disk also suggests a magnetic field component with a scale height significantly smaller than the eDIG scale height(s), a potentially unstable configuration in which the gas layer would “float” atop the magnetic field.

We determine the magnetic field and cosmic-ray pressure gradients via the energy equipartition assumption despite increasing indications for departures from equipartition in a range of environments (e.g., Schmidt 2016; Yoast-Hull et al. 2016). We also must make simplifying assumptions about the cylindrical geometry and radial extent of the eDIG layer that affect our estimates of the electron density profile. While adjustments to any of these assumptions could affect the success of the dynamical equilibrium model, its failure in two galaxies with disparate properties builds confidence that this model is a poor description of the dynamical state of eDIG layers.

Given the failure of the dynamical equilibrium model, we can ask what evidence exists for nonequilibrium models of the gaseous, disk-halo interface. The eDIG emission-line ratios suggest that the gas is chemically enriched. This implies that the eDIG is either directly transported out of the disk or originates in a disk-halo circulation that triggers thermal instabilities in the lower halo. Chemically-enriched, warm gas may arise through cooling in the wakes of cool clouds traveling through the hot halo if either the halo itself is enriched or the clouds sufficiently enrich their wakes (see, e.g., Marasco et al. 2012). Careful study of chemical abundances inferred from emission-line ratios may shed light on the extent to which such “induced” accretion contributes to the eDIG layer in NGC 5775. Regardless, the evidence suggests that the low-angular-momentum gas originates in a disk-halo flow rather than through direct accretion from a metal-poor, intergalactic reservoir.

We discuss the two most commonly considered disk-halo flows - galactic fountains and galactic winds - here. We favor the former scenario for several reasons. First, we do not see evidence for a traditional outflow cone in the eDIG kinematics. If such a cone exists, it must have an unusually small opening angle that directs the outflow away from our line of sight. Although the symmetric, blueshifted gas at large  $z$  along the minor axis hints at an outflow, it lacks the redshifted component that we expect to arise from an outflow cone and has a line-of-sight velocity well below the escape velocity. If an outflow is present in the hot phase of the halo, as suggested by the X-shaped field geometry (Soida et al. 2011), then a small volume filling factor would likely be required for the eDIG layer to avoid entrainment of the warm gas.

Thus, we favor a galactic fountain flow in which eDIG clouds circulate between the disk and the halo. The blueshifted gas at large  $z$  along the minor axis may be evidence of such a circulation. We may only observe the outflow stage of the fountain flow if the gas is primarily in a warm, ionized phase during this stage. However, this is somewhat at odds with the conventional picture in which gas clouds leave the disk in a hot ionized phase

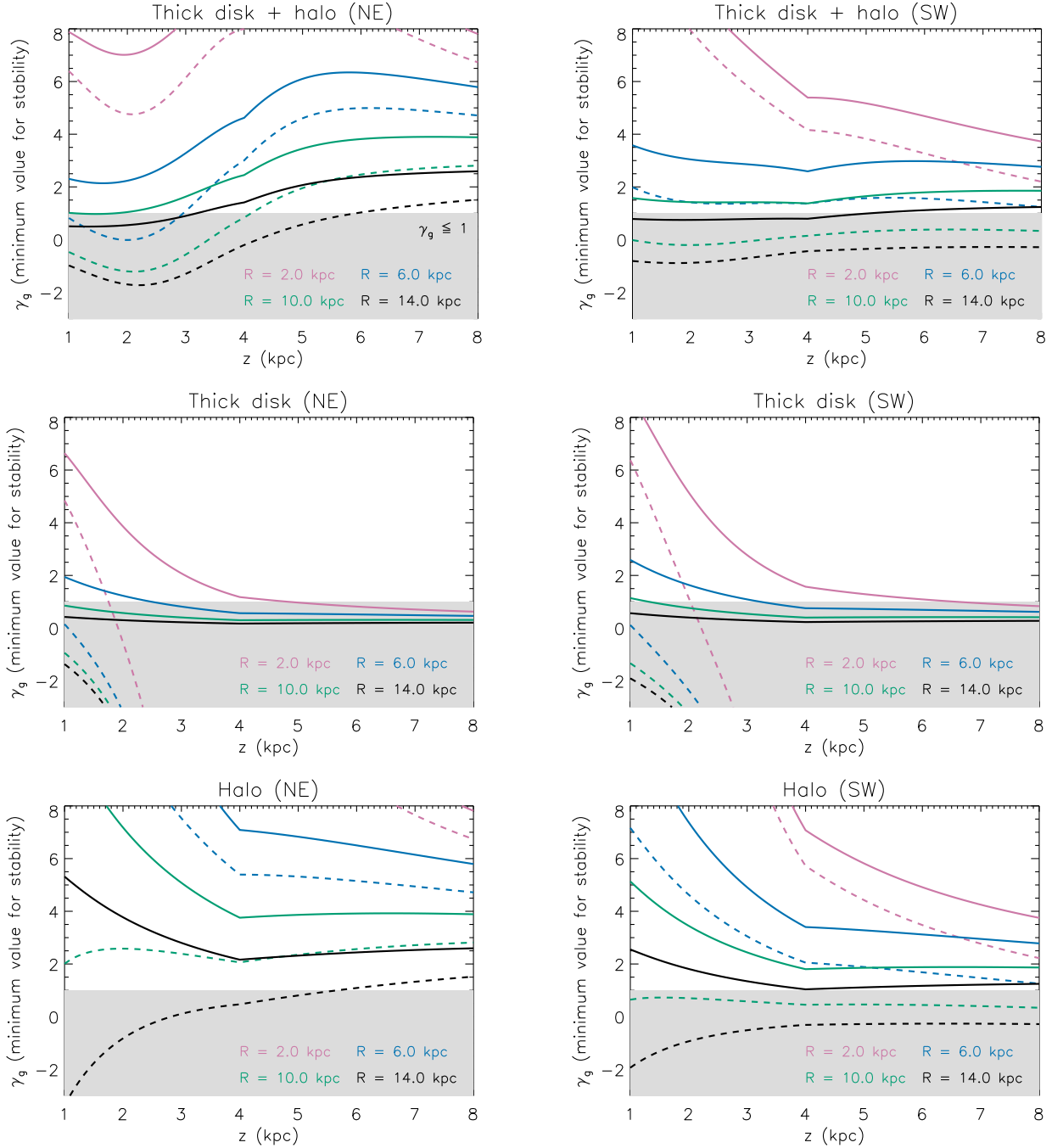


FIG. 10.— Minimum value of  $\gamma_g$  required to satisfy the Parker stability criterion for the eDIG layer at a range of galactocentric radii. Solid and dashed lines are derived assuming  $\gamma_{cr} = 0$  and  $\gamma_{cr} = 1.45$ . Models within the shaded region satisfy the conservative criterion that the minimum  $\gamma_g$  required for stability be  $\gamma_g \leq 1$ . This requirement is only satisfied at all  $z$  for  $\gamma_{cr} = 1.45$ , and even then only at large galactocentric radii (generally  $R \geq 6$  kpc). The Parker instability thus further restricts the success of the dynamical equilibrium model to moderate and large galactocentric radii.

and return to the midplane in a warm ionized or neutral state. An alternative explanation is that the kinematics observed along the minor axis are dominated by a local feature such as a filament that is primarily outflowing from the disk. However, no such filament is obvious in the H $\alpha$  imaging of Collins et al. (2000).

We also consider whether the interaction with NGC 5774 has influenced the kinematics of extraplanar gas in NGC 5775. There is no obvious evidence of interaction in any of the slit locations; most notably, s2 produces a rotation curve characteristic of noninteracting galaxies despite sampling the side of the galaxy where the HI bridge connects the companion galaxies. However, the question of whether the blueshifted gas along the minor axis could arise from ram pressure is intriguing. If the interaction has deposited comparatively dense gas in the path of NGC 5775, then passage through this gas could sweep the halo of NGC 5775 toward the observer as the galaxy recedes. Although the HI kinematics of the NGC 5775 - NGC 5774 system are potentially consistent with this scenario (Irwin 1994), more detailed modeling is needed to assess the effects of ram pressure on the gaseous halo. We also note that such effects are not necessary to interpret the kinematics observed off of the minor axis in this work and others (e.g., Rand 2000).

It is clear that the current observations do not provide a fully definitive description of the dynamical state of the eDIG layer in NGC 5775. However, they suggest a most likely scenario. The interaction of NGC 5775 with NGC 5774, while not directly shaping the kinematics of extraplanar gas in the inner disk, has enhanced the star-formation rate in the former galaxy and thus helped give rise to the vertically-extended, multiphase gaseous halo. The warm, ionized phase has a multicomponent vertical density distribution that is most likely sustained via a galactic fountain flow between the disk and the halo. The observed increase in the velocity dispersion as a function of height is a natural consequence of this model if the gas clouds are ejected from the disk with a range of velocities; in this model, the clouds with the highest dispersion will naturally reach the largest scale heights. The evidence for shock heating and ionization in the emission-line ratios is consistent with this turbulent, multiphase medium. We discuss future observations to explore this interpretation in the conclusions below.

## 6. SUMMARY AND CONCLUSIONS

We combined optical and NUV emission-line spectroscopy from RSS on SALT with radio continuum observations from CHANG-ES to study the dynamical state of the eDIG layer in NGC 5775. We summarize the main results of our study here:

- The exponential electron density distribution has both thick disk and halo components and is asymmetric on the northeast and southwest sides of the galaxy. The scale heights of these components are  $h_{z,e} = 0.6$  and  $7.5$  kpc on the northeast and  $h_{z,e} = 0.8$  and  $3.6$  kpc on the southwest sides, showing the remarkable spatial extent of the warm ionized halo.
- We observe evidence of a previously-detected rotational velocity gradient characteristic of lagging halos (e.g., Heald et al. 2006). We report

line-of-sight velocity gradients as high as  $\Delta v = -25$  km s $^{-1}$  kpc $^{-1}$  in some locations, although quantification of the true *rotational* velocity gradient is beyond the scope of this work.

- The H $\alpha$  velocity dispersion displays a significant increase from  $\sigma_{H\alpha} = 20$  km s $^{-1}$  at  $z = 0$  kpc to  $\sigma_{H\alpha} = 60$  km s $^{-1}$  at  $|z| = 4$  kpc, where the dispersion appears to plateau. This is the first clear evidence for a rising velocity dispersion as a function of height in an eDIG layer.
- The thermal, turbulent, magnetic field, and cosmic-ray pressure gradients are insufficient to support the gas in dynamical equilibrium at its observed scale height except at large galactocentric radii ( $R \geq 11$  kpc for the sum of all density components). Success of this model thus requires a ring geometry inconsistent with observations of face-on galaxies.
- In the context of the dynamical equilibrium model, we assess the stability of the eDIG layer against the well-known Parker instability. While the thick-disk component is largely stable if the cosmic rays are coupled to the gas ( $\gamma_{cr} = 1.45$ ), the halo component on the northeast side is not stable at all  $z$  over the range of galactocentric radii considered ( $R \leq 14$  kpc).
- The emission-line ratios display smooth trends from the disk to the halo consistent with increased heating of uniform-metallicity gas at large  $z$ . This suggests a disk origin for the gas; if the eDIG is evidence of accretion activity, it must arise from an enriched halo.
- There is no obvious evidence of interaction between NGC 5775 and NGC 5774 in the kinematics of the extraplanar gas. It appears that the main influence of the interaction on the thick-disk ISM of NGC 5775 is to trigger the star formation that gives rise to the multiphase, gaseous halo.
- At large  $z$  along the minor axis, the gas is blueshifted on both sides of the midplane by a few tens of km s $^{-1}$ . We discuss possible explanations for this observation, including outflowing gas in a multiphase fountain flow and ram pressure effects from the interaction with NGC 5774.
- This and previous works indicate the need for a supplemental source of heating and/or ionization that behaves differently from photoionization in the eDIG layer of NGC 5775. The extended, co-spatial thermal and nonthermal halos in this galaxy, as well as evidence that cosmic-ray heating may be important (Wiener et al. 2013), motivate further study of the role of cosmic rays in the energy balance and ionization state of the eDIG.

As discussed in §5, past and current observations of the eDIG layer in NGC 5775 are most consistent with a non-hydrostatic, galactic fountain flow. Turbulent, multiphase gas clouds ejected from the disk reach scale heights characteristic of their ejection energies, possibly passing

through phase transitions that obscure some stages of this process in the optical. Shock heating and/or ionization evidenced by trends in emission-line ratios are consistent with the interaction of ejected clouds with the ambient medium. In this picture, the gas in the eDIG layer both originates in and returns to the disk and thus is not indicative of a substantial transfer of baryons or metals between the disk and the environment. Enriching and cooling of hot halo gas as cool clouds travel through the lower halo may, however, contribute to the presence of warm, ionized gas at the disk-halo interface.

To further test this interpretation, we suggest future observations to shed light on several open questions about the eDIG layer in this and similar systems. In NGC 5775, the remarkable vertical extent of the gaseous halo in emission is intriguing. It is not yet clear that we have detected the full vertical extent in emission, nor have we definitely determined the number of exponential electron density components. Deep, ground-based, narrow-band imaging that prioritizes both the field of view and quality sky subtraction would help to achieve these goals, furthering our understanding of the fraction of halo gas mass found in the warm, ionized phase.

Additionally, interpretation of intriguing kinematic results such as the blueshifted gas at high  $z$  along the minor axis is challenging with the limited spatial coverage of longslit spectroscopy. Integral field unit and/or Fabry-Perot spectroscopy would enable analysis of gas kinematics over greatly improved fields of view, an effort begun for this galaxy by Heald et al. (2006). We propose additional observations with improved sensitivity in order to probe the kinematics at  $|z| \geq 4$  kpc in a spatially-resolved fashion. Such observations would enable discrimination between outflow and ram pressure origins for the minor axis kinematics as discussed in §5. In the modeling regime, improved models of cosmic-ray transport will advance our understanding of the validity of the energy equipartition assumption in assessing nonthermal pressure gradients in gaseous halos (e.g., Schmidt 2016).

Finally, it is clear that edge-on galaxies alone will not fully illuminate the vertical structure, support, and kinematics of eDIG layers. Ongoing efforts to study the vertical bulk velocities and velocity dispersions in low-inclination galaxies will be a powerful complement to the high-inclination perspective (e.g., Boettcher et al. 2017), allowing more rigorous testing of the ideas discussed here.

All of the observations reported in this paper were obtained with the Robert Stobie Spectrograph (RSS) on the Southern African Large Telescope (SALT) under programs 2015-1-SCI-023 and 2016-2-SCI-029 (PI: E. Boettcher). We thank the SALT astronomers and telescope operators for obtaining the observations and Petri Vaisanen for advice on data acquisition. We acknowledge Ken Nordsieck for his expertise on the RSS instrument and Arthur Eigenbrot for his help with data reduction. We thank Bob Benjamin, Rainer Beck, George Heald, Dick Henriksen, Judith Irwin, Jiang-Tao Li, Richard Rand, Carlos Vargas, and Rene Walterbos for useful discussions and comments. We acknowledge Masataka Okabe and Kei Ito for supplying the colorblind-friendly color palette used in this paper (see

[fly.iam.u-tokyo.ac.jp/color/index.html](http://fly.iam.u-tokyo.ac.jp/color/index.html)).

This material is based upon work supported by the National Science Foundation Graduate Research Fellowship Program under Grant No. DGE-1256259. Any opinions, findings, and conclusions or recommendations expressed in this material are those of the author(s) and do not necessarily reflect the views of the National Science Foundation. Support was also provided by the Graduate School and the Office of the Vice Chancellor for Research and Graduate Education at the University of Wisconsin-Madison with funding from the Wisconsin Alumni Research Foundation.

This work has made use of NASA’s Astrophysics Data System and of the NASA/IPAC Extragalactic Database (NED) which is operated by the Jet Propulsion Laboratory, California Institute of Technology, under contract with the National Aeronautics and Space Administration.

## 7. APPENDIX

### 7.1. Example Spectra and Gaussian Fits

In Fig. 11, we show example spectra from the minor axis on the northeast side of the galaxy (s1). In the top panel, the Gaussian fits for detected H $\alpha$  and [NII] $\lambda$ 6583 lines are shown; the corresponding residuals are given in the bottom panel. In general, the emission-line profiles are well characterized by a single Gaussian fit. However, at high S/N, low- and/or high-velocity wings are apparent in some locations. This is particularly evident for the red wing seen in both the H $\alpha$  and [NII] residuals at  $z = 1.2$  kpc. While detection of such wings is challenging at high  $|z|$  due to the low S/N, the detection of these wings at low  $|z|$  suggests the presence of gas at more extreme velocities than are considered in this work. Higher S/N spectra that can better characterize the emission-line wings would help to determine whether there is an additional, low-surface-brightness component with a higher velocity dispersion than quantified here.

We provide the best-fit Gaussian parameters in machine-readable tables available online (see Tab. 4 - 7). Portions of these tables are given below for guidance with respect to their form and content.

### 7.2. A Mass Model for NGC 5775

To determine the galactic gravitational potential of NGC 5775, we follow Collins et al. (2002) in adopting the mass model presented in the Appendix of Wolfire et al. (1995). This model consists of a disk, spherical bulge, and logarithmic halo; although it is developed for the Galaxy, it can be adapted to other systems by adjusting the  $v_{circ}$  parameter. We take  $v_{circ} = 195$  km s $^{-1}$  to match the HI rotation curve of NGC 5775 (Irwin 1994), and we compare the adapted Wolfire et al. (1995) and Irwin (1994) rotation curves in Fig. 12. The rotation curves are in good agreement at large  $R$ ; discrepancy at small  $R$  may be due to lack of HI in the inner part of the galaxy. For the disk, bulge, and halo components, the gravitational potential,  $\Phi(z, R)$ , and the gravitational acceleration,  $-g_z = -\frac{d\Phi(z, R)}{dz}$ , are given in Eq. (A1) - (A3) and (A7) - (A9) of Wolfire et al. (1995).

TABLE 4  
BEST-FIT EMISSION-LINE PROPERTIES: S1

$z$ (kpc)	$I_{H\alpha}$ ( $10^{-17}$ erg $\text{cm}^{-2}$ $\text{s}^{-1}$ arcsec $^{-2}$ )	$v_{H\alpha}$ <sup>a</sup> (km $\text{s}^{-1}$ )	$\sigma_{H\alpha}$ <sup>b</sup> (km $\text{s}^{-1}$ )	$\frac{[OI]\lambda 6300}{H\alpha}$	$v_{[OI]}$ (km $\text{s}^{-1}$ )	$\sigma_{[OI]}$ (km $\text{s}^{-1}$ )	... <sup>c</sup>
8.1	$0.5 \pm 0.1$	$1637 \pm 7$	$42 \pm 7$	0	0	0	...
...	...	...	...	...	...	...	...

<sup>a</sup> The heliocentric radial velocity.

<sup>b</sup> The line width corrected for the spectral resolution.  $\sigma$  refers to the standard deviation and not the FWHM of the Gaussian fit.

<sup>c</sup> The remaining columns give the line ratio with respect to  $H\alpha$ , velocity, and velocity dispersion for the  $[NII]\lambda 6583$  and  $[SII]\lambda 6717$  lines. Null entries indicate locations where the relevant emission line was not detected. This table is available in its entirety in machine-readable form.

TABLE 5  
BEST-FIT EMISSION-LINE PROPERTIES: S2

$R$ (kpc)	$I_{H\alpha}$ ( $10^{-17}$ erg $\text{cm}^{-2}$ $\text{s}^{-1}$ arcsec $^{-2}$ )	$v_{H\alpha}$ <sup>a</sup> (km $\text{s}^{-1}$ )	$\sigma_{H\alpha}$ <sup>b</sup> (km $\text{s}^{-1}$ )	$\frac{[NII]\lambda 6583}{H\alpha}$	$v_{[NII]}$ (km $\text{s}^{-1}$ )	$\sigma_{[NII]}$ (km $\text{s}^{-1}$ )	... <sup>c</sup>
13.5	$1.1 \pm 0.1$	$1532 \pm 5$	$46 \pm 5$	0	0	0	...
...	...	...	...	...	...	...	...

<sup>a</sup> The heliocentric radial velocity.

<sup>b</sup> The line width corrected for the spectral resolution.  $\sigma$  refers to the standard deviation and not the FWHM of the Gaussian fit.

<sup>c</sup> The remaining columns give the line ratio with respect to  $H\alpha$ , velocity, and velocity dispersion for the  $[SII]\lambda 6717$  line. Null entries indicate locations where the relevant emission line was not detected. This table is available in its entirety in machine-readable form.

TABLE 6  
BEST-FIT EMISSION-LINE PROPERTIES: S3UV

$z$ (kpc)	$I_{[OII]}$ (SALT ADU)	$\frac{[OII]\lambda 3729}{[OII]\lambda 3726}$	$v_{[OII]}$ <sup>a</sup> (km $\text{s}^{-1}$ )	$\sigma_{[OII]}$ <sup>b</sup> (km $\text{s}^{-1}$ )
5.8	$11 \pm 9$	$2.0^{+0.83}_{-0.83}$	$1651^{+16}_{-16}$	$30^{+26}_{-16}$
...	...	...	...	...

<sup>a</sup> The heliocentric radial velocity.

<sup>b</sup> The line width corrected for the spectral resolution.  $\sigma$  refers to the standard deviation and not the FWHM of the Gaussian fit. This table is available in its entirety in machine-readable form.

TABLE 7  
BEST-FIT EMISSION-LINE PROPERTIES: S3O

$z$ (kpc)	$I_{H\alpha}$ (SALT ADU)	$v_{H\alpha}$ <sup>a</sup>	$\frac{[OII]\lambda 3727}{H\alpha}$	$\frac{[OIII]\lambda 5007}{H\alpha}$	$\frac{[OI]\lambda 6300}{H\alpha}$	$\frac{[NII]\lambda 6583}{H\alpha}$
8.1	$96 \pm 17$	$1714 \pm 23$	0	0	0	0
...	...	...	...	...	...	...

<sup>a</sup> The heliocentric radial velocity. Null entries indicate locations where the relevant emission line was not detected. This table is available in its entirety in machine-readable form.

## REFERENCES

- Asplund, M., Grevesse, N., Sauval, A. J., et al. 2009, *ARA&A*, 47, 481
- Beck, R. 2015, *A&A Rev.*, 24, 4
- Boettcher, E., Gallagher, III, J. S., & Zweibel, E. G. 2017, *ApJ*, 845, 155
- Boettcher, E., Zweibel, E. G., Gallagher, III, J. S., & Benjamin, R. A. 2016, *ApJ*, 832, 118
- Boulares, A., & Cox, D. P. 1990, *ApJ*, 365, 544
- Brar, R. S., Irwin, J. A., & Saikia, D. J. 2003, *MNRAS*, 340, 269
- Bregman, J. N. 1980, *ApJ*, 236, 577
- Buckley, D. A. H., Swart, G. P., & Meiring, J. G. 2006, in *Proc. SPIE*, Vol. 6267, Society of Photo-Optical Instrumentation Engineers (SPIE) Conference Series, 62670Z
- Burgh, E. B., Nordsieck, K. H., Kobulnicky, H. A., et al. 2003, in *Proc. SPIE*, Vol. 4841, Instrument Design and Performance for Optical/Infrared Ground-based Telescopes, ed. M. Iye & A. F. M. Moorwood, 1463
- Cardelli, J. A., Clayton, G. C., & Mathis, J. S. 1989, *ApJ*, 345, 245
- Collins, J. A., Benjamin, R. A., & Rand, R. J. 2002, *ApJ*, 578, 98
- Collins, J. A., & Rand, R. J. 2001, *ApJ*, 551, 57
- Collins, J. A., Rand, R. J., Duric, N., & Walterbos, R. A. M. 2000, *ApJ*, 536, 645
- Crawford, S. M., Still, M., Schellart, P., et al. 2010, in *Proc. SPIE*, Vol. 7737, Observatory Operations: Strategies, Processes, and Systems III, 773725

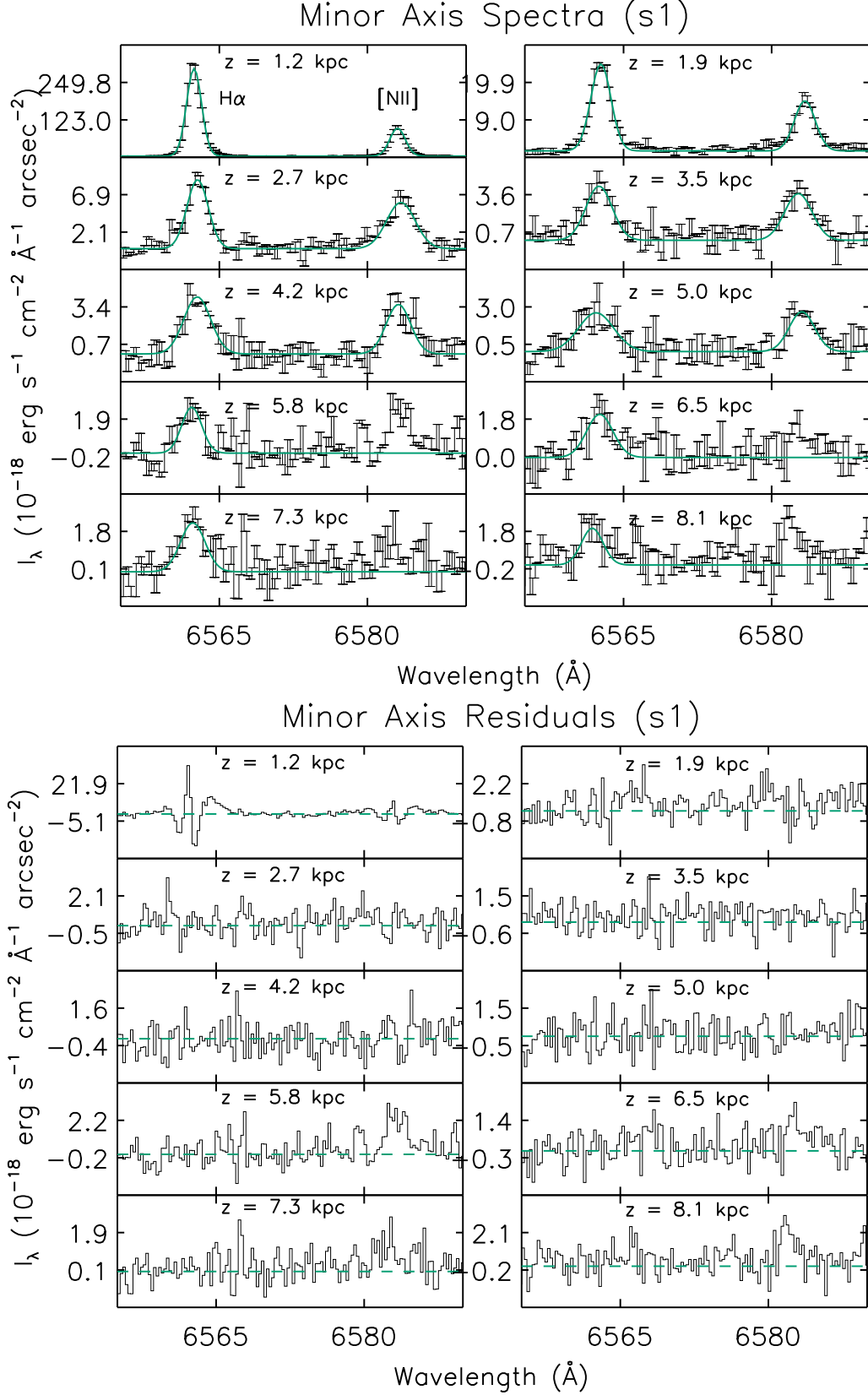


FIG. 11.— Example rest-frame spectra along the minor axis on the northeast side of the galaxy (s1). Gaussian fits and their residuals are shown in the top and bottom panels, respectively. Fits are shown for the H $\alpha$  and [NII] $\lambda$ 6583 lines that meet our detection criteria.

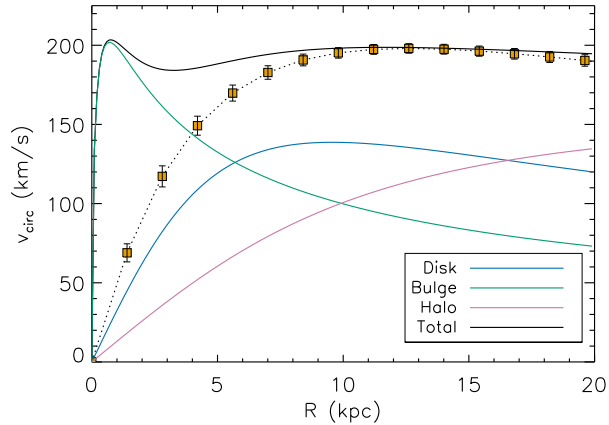


FIG. 12.— Galactic rotation curve of Wolfire et al. (1995) adapted to NGC 5775 (solid lines) compared to the modeled HI rotation curve of Irwin (1994) (yellow squares).

de Vaucouleurs, G., de Vaucouleurs, A., Corwin, Jr., H. G., et al. 1991, *Third Reference Catalogue of Bright Galaxies, Vol. I: Explanations and references. Vol. II: Data for galaxies between  $0^h$  and  $12^h$ . Vol. III: Data for galaxies between  $12^h$  and  $24^h$ .* (New York, NY: Springer)

Dettmar, R.-J. 1990, *A&A*, 232, L15

Duric, N., Irwin, J., & Bloemen, H. 1998, *A&A*, 331, 428

Ferrière, K. M. 2001, *Reviews of Modern Physics*, 73, 1031

Fletcher, A., & Shukurov, A. 2001, *MNRAS*, 325, 312

Franco, J., Ferrini, F., Ferrara, A., & Barsella, B. 1991, *ApJ*, 366, 443

Fraternali, F., & Binney, J. J. 2006, *MNRAS*, 366, 449

Haffner, L. M., Reynolds, R. J., & Tufte, S. L. 1998, *ApJ*, 501, L83

—. 1999, *ApJ*, 523, 223

Heald, G. H., Rand, R. J., Benjamin, R. A., Collins, J. A., & Bland-Hawthorn, J. 2006, *ApJ*, 636, 181

Heintz, E., & Zweibel, E. G. 2018, *ApJ*, 860, 97

Hill, A. S., Jounge, M. R., Mac Low, M.-M., et al. 2012, *ApJ*, 750, 104

Irwin, J., Beck, R., Benjamin, R. A., et al. 2012, *AJ*, 144, 43

Irwin, J. A. 1994, *ApJ*, 429, 618

Kobulnicky, H. A., Nordsieck, K. H., Burgh, E. B., et al. 2003, in *Proc. SPIE, Vol. 4841, Instrument Design and Performance for Optical/Infrared Ground-based Telescopes*, ed. M. Iye & A. F. M. Moorwood, 1634

Krause, M., Irwin, J., Wiegert, T., et al. 2018, *A&A*, 611, A72

Larson, R. B., Tinsley, B. M., & Caldwell, C. N. 1980, *ApJ*, 237, 692

Lee, S.-W., Seaquist, E. R., Leon, S., et al. 2002, *ApJ*, 573, L107

Lehnert, M. D., & Heckman, T. M. 1995, *ApJS*, 97, 89

Li, J.-T., Li, Z., Wang, Q. D., Irwin, J. A., & Rossa, J. 2008, *MNRAS*, 390, 59

Li, J.-T., & Wang, Q. D. 2013, *MNRAS*, 428, 2085

Marasco, A., Fraternali, F., & Binney, J. J. 2012, *MNRAS*, 419, 1107

Newcomb, W. A. 1961, *Physics of Fluids*, 4, 391

Osterbrock, D. E., & Ferland, G. J. 2006, *Astrophysics of Gaseous Nebulae and Active Galactic Nuclei* (Sausalito, CA: Univ. Science Books)

Otte, B., Gallagher, III, J. S., & Reynolds, R. J. 2002, *ApJ*, 572, 823

Parker, E. N. 1966, *ApJ*, 145, 811

Rand, R. J. 1997, *ApJ*, 474, 129

—. 1998, *ApJ*, 501, 137

—. 2000, *ApJ*, 537, L13

Rand, R. J., Wood, K., Benjamin, R. A., et al. 2011, *ApJ*, 728, 163

Reynolds, R. J., Hausen, N. R., Tufte, S. L., & Haffner, L. M. 1998, *ApJ*, 494, L99

Rossa, J., & Dettmar, R.-J. 2003, *A&A*, 406, 493

Schlafly, E. F., & Finkbeiner, D. P. 2011, *ApJ*, 737, 103

Schmidt, P. 2016, PhD thesis, University of Bonn

Sembach, K. R., Howk, J. C., Ryans, R. S. I., & Keenan, F. P. 2000, *ApJ*, 528, 310

Shapiro, P. R., & Field, G. B. 1976, *ApJ*, 205, 762

Silk, J. 2003, *MNRAS*, 343, 249

Soida, M., Krause, M., Dettmar, R.-J., & Urbanik, M. 2011, *A&A*, 531, A127

Tremonti, C. A., Heckman, T. M., Kauffmann, G., et al. 2004, *ApJ*, 613, 898

Tüllmann, R., Dettmar, R.-J., Soida, M., Urbanik, M., & Rossa, J. 2000, *A&A*, 364, L36

Tüllmann, R., Pietsch, W., Rossa, J., Breitschwerdt, D., & Dettmar, R.-J. 2006, *A&A*, 448, 43

van Dokkum, P. G. 2001, *PASP*, 113, 1420

Veilleux, S., Cecil, G., & Bland-Hawthorn, J. 2005, *ARA&A*, 43, 769

Wiegert, T., Irwin, J., Miskolczi, A., et al. 2015, *AJ*, 150, 81

Wiener, J., Zweibel, E. G., & Oh, S. P. 2013, *ApJ*, 767, 87

Wolfire, M. G., Hollenbach, D., McKee, C. F., Tielens, A. G. G. M., & Bakes, E. L. O. 1995, *ApJ*, 443, 152

Yoast-Hull, T. M., Gallagher, J. S., & Zweibel, E. G. 2016, *MNRAS*, 457, L29

Zweibel, E. G. 2013, *Physics of Plasmas*, 20, 055501

Zweibel, E. G., & Kulsrud, R. M. 1975, *ApJ*, 201, 63